Università degli Studi di Ferrara

DOTTORATO DI RICERCA IN FISICA, XXV ciclo
Coordinatore Prof. Vincenzo Guidi

Spin Coherence Time studies for the storage ring EDM search

Dottoranda:
Guidoboni Greta

Relatore:
Dott. Lenisa Paolo

Anni 2010-2012

Contents

Introduction **III**

1 The elctric dipole moment **1**

1.1 Baryon asymmetry 1

1.2 CP violation in the SM and beyond 2

1.3 The EDM as probe of new physics 4

1.3.1 Theoretical predictions 5

1.3.2 Experiments 6

1.4 EDM search in storage rings 8

2 Elements of accelerator physics **11**

2.1 Transverse beam dynamics 11

2.1.1 Strong focusing 11

2.1.2 Equation of motion 12

2.1.3 Momentum dispersion 16

2.2 Longitudinal beam dynamics 18

2.2.1 Phase stability 18

2.2.2 Equation of motion 20

3 The COSY storage ring **23**

3.1 Experimental techniques and setup 25

3.1.1 Polarization measurement 25

3.1.2 EDDA polarimeter 28

3.2 Data Acquisition 30
3.2.1 Vertical polarization measurement 30
3.2.2 Horizontal polarization measurement 30

4 Study of an rf-solenoid spin resonance 35
4.1 Machine parameters and measurements 37
4.2 Spin tracking model 38
4.3 Data analysis 41
4.3.1 Model parameters 41
4.3.2 Synchrotron oscillation effects 45
4.3.3 Resonance shape 50
4.4 Conclusions 53

5 Spin Coherence Time measurements 55
5.1 Exprimental setup 55
5.2 Extracting spin coherence time 56
5.3 Emittance effects 61
5.4 Sextupole corrections 64
5.5 Conclusions 66

6 Conclusions 69

Bibliography 74

Introduction

The present work has been developed within the framework of the project to measure the Electric Dipole Moment (EDM) of charged particles in a storage ring. The measurements presented here were made at the COSY (COoler SYnchrotron) ring located at the Forschungszentrum-Jülich GmbH (Germany).

The measurement of a non-zero EDM aligned with the spin of fundamental particles would contribute to solving one of the puzzles of contemporary physics, the so-called baryon asymmetry, that asks why matter dominates over anti-matter in our universe. According to the Big Bang Theory, at the origin of the universe an equal amount of matter and anti-matter was present. This symmetry must have been broken by mechanisms violating charge symmetry C and the combined charge-parity symmetry CP under conditions far from thermal equilibrium (see Sakharov's criteria). Despite the fact that the Standard Model contains all these elements, it is not able to explain the size of the current baryon asymmetry, especially because the amount of CP violation (essentially coming from the weak sector) is too small. This CP violation is scaled to match the observed cross sections in the decay of K-meson and B-meson. What is needed is a window that would allow us to observe new forms of CP violation. One way to proceed is to measure the time-reversal violation determined by the size of an EDM aligned with the spin of a particle, nucleon, or atomic system.

The EDM is a charge displacement that lies along the particle's spin axis. Under a parity transformation P which inverts the spacial coordinates, the spin direction remains unchaged while the EDM flips. Under a time reversal operation T which inverts the time coordinate, the EDM stays the same and the spin direction is inverted. The failure of either transformation to reproduce the original system indicates that the presence of an EDM along the particle's axis represents a violation of both parity and time-reversal symmetries. Assuming the conservation of the combined symmetries CPT, a violation of T represents a violation of CP. Thus time reversal violation experiments represent a way to look for CP violation aside from comparing particle and anti-particle reaction rates.

The theoretical predictions based on multi-loop Standard Model mechanisms (e.g. neutron $|\vec{d_n}| \sim 10^{-34}$ e·cm) are several orders of magnitude below the current EDM experimental limits ($|\vec{d_n}| \sim 10^{-26}$e·cm). In contrast, models beyond the Standard Model forsee EDMs well within the planned experimental precision. The measurement of a non-vanishing EDM at the sensitivity of present or planned experiments would clearly prove the existence of new CP violating meachanisms beyond the Standard Model.

Noting that the first CP non-invariance was observed in K-meson decay in 1964, the question of the symmetry properties of fundamental forces or particles was put forward by Purcell and Ramsey in 1951. They searched unsuccessfully for a parity-violating up-down asymmetry in the scattering of neutrons from nuclei. Even if they were not explicity looking for an EDM, their work is usually recalled as the first EDM experiment. After that, the EDM search intensified and the level of experimental precision has improved steadily ever since, now including heavy atoms and molecules as well as neutrons. For a neutral system, the usual method for detecting the EDM $\vec{d}$ is to apply an electric field $\vec{E}$ and look for the energy shift $\vec{d} \cdot \vec{E}$. Unfortunately, this method cannot be used for charged particles which would be accelerated by the electric field and then lost.

The development of storage ring technology and polarized beams made possible the recent proposal to measure the EDM of charged particles. The proposed solution is the use of a storage ring where the polarized charged particle beam can be kept circulating while interacting with the radial electric field always present in the particle frame. Starting with a longitudinally polarized beam (particle spins aligned along the velocity), the EDM signal would be detected as a polarization precession starting from the horizontal plane and rotating toward the vertical direction.

There are two fundamental conditions to fulfill in order to realize this experiment. One is freezing the polarization precession frequency in the horizontal plane to the revolution frequency of the beam in the ring, so that the beam will be always longitudinally polarized. The second condition is to guarantee a long horizontal polarization lifetime which defines the observation time available to measure the EDM signal.

A deep comprehension of beam and spin dynamics in a storage ring is needed to study the feasibility of the proposed EDM experiment for charged particles. In particular, the understanding of spin dynamics is a crucial point in order to provide a long horizontal polarization lifetime. The stable spin axis in a storage ring is along the vertical axis, orthogonal to the ring plane. Thus, as soon as a spin moves out from the stable direction, it will start precessing around it with a frequency proportional to the relativistic factor γ of its motion and the local magnetic field. The number of spin precessions per turn around a storage ring is called the *spin tune*. Since particles have slightly different velocities, the spins will precess with different frequencies, spreading around in the horizontal plane and making the horizontal polarization shrink and vanish. The horizontal polarization lifetime represents the obervation time available to detect the EDM signal and is called the *spin coherence time*. The goal for the deuteron EDM experiment is to achieve an EDM sensitivity of 10^{-29} e·cm, which requires a spin coherence time of at least 1000 s along with the ability to measure microradians of polarization rotation.

The aim of this work is the analysis of the mechanisms which control the spin coherence time in a storage ring as a part of the feasibility studies for the deuteron EDM experiment. For this reason a series of dedicated studies has been started at the COSY ring in Jülich. The COSY ring provides beams of polarized protons and deuterons in a momentum range from 300 MeV/c to 3.7 GeV/c. Beam polarimetry tools are also available, such as the LEP (Low Energy Polarimeter) to measure the polarization of the states injected and the EDDA scintillator detectors used as a mock EDM polarimeter.

A first set of measurements was devoted to study the spin coherence time in presence of a radio-frequency (rf) solenoid induced spin resonance. Since the width of this resonance depends on the spin tune spread and thus on the particle momentum distribution, it represents a good starting point to estimate the size of the spin tune spread before moving to a direct measurement of the spin coherence time. A vertically polarized deuteron beam was injected in COSY and accelerated to a momentum of 0.97 GeV/c.

A continuous polarization measurement was provided by slowly extracting the beam into a thick carbon target and detecting the elastically scattered deuterons in the EDDA polarimeter. The use of electron-cooled and uncooled beams permitted observation of the effect of momentum spread and beam size on the polarization while running the rf-solenoid either at fixed or variable frequency. In order to analyze the data, I developed a "no lattice" model together with Dr. E. J. Stephenson, based on two matrices to decribe the spin precession about the vertical axis and the spin rotation due to the solenoid effect.

The second experiment was devoted to the measurement of the horizontal polarization lifetime as a function of time. It required the development of a dedicated data acquisition system aimed at detecting the precession of the horizontal polarization as a function of time. Data were analyzed using a set of template curves which allowed the study the contribution of beam emittance (transverse beam size) to the spin coherence time. Then, it was succesfully verifed the possibility to correct emittance effects on the spin tune spread using sextupole magnets, obtaining a longer spin coherence time.

The thesis is divided in six chapaters:

- *Chapter 1* yields a theoretical overview of the EDM as probe of new physics including the experimental results achieved up to now. The new method for the measurement of a charged particle EDM in a storage ring closes the chapter.

- *Chapter 2* provides the basic elements of beam dynamics in a storage ring which are necessary to understand the analysis and the measurements presented in the thesis.

- *Chapter 3* describes the COSY storage ring where the experiments have been conducted. It contains the definition of polarization for a spin-1 particle such as the deuteron and the methods to measure it.
- *Chapter 4* illustrates the first set of measurements which focus on the effects of synchrotron oscillations on the vertical polarization and the "no lattice model" used for the analysis.
- *Chapter 5* shows the direct measurement of horizontal polarization as a function time including the emittance effects and the sextupole corrections to the depolarization with time.
- *Chapter 6* contains a summary describing what has been achieved and the prospects for future developments.

Chapter 1

The Electric Dipole Moment as a probe of CP violation

1.1 Baryon asymmetry

In cosmology, an important fact still lacking explanation is the existence of the large amount of matter which forms the galaxies, the stars and the interstellar medium. There is essentially no antimatter in a universe that started with no particle content right after inflation. This chapter will explore how this problem of baryogenesis is linked to the possible existence of an electric dipole moment (EDM) aligned along the spin axis of particles. All explanations of baryogenesis in the early universe necessarily require a significant amount of CP violation, the combination of charge conjugation and parity symmetries, that is a characteristic of an EDM.

The matter content of the universe usually is quantified by the ratio of the number density of baryons n_b to the number density of photons n_γ, also called the asymmetry parameter, which is:

$$\eta = n_b/n_\gamma = (6.08 \pm 0.14) \times 10^{-10} \tag{1.1}$$

as the derived from the CMB saltellite data and from primordial nucleosynthesis data [1]. At the present temperature $T = 2.728 \pm 0.004$ K of the universe, the photon number density is $n_\gamma = 405$ cm^{-3}. There is strong evidence that the universe consists entirely of matter, as opposed to antimatter, and the few antiprotons $n_{\bar{p}}/n_p \sim 10^{-4}$ seen in cosmic rays can be explained by secondary pair production processes.

The predicted number of baryons and antibaryons is minuscule, $n_b/n_\gamma =$

$n_{\bar{b}}/n_\gamma \sim 10^{-18}$, which for baryons is more than 8 orders of magnitude below the observed value (see Eq. 1.1). The process responsible for this unexpectedly large baryon asymmetry of the universe, generated from an initially symmetric configuration, is called baryogenesis.

The general criteria which allow for the dynamical generation of a baryon asymmetry from an initial baryo-symmetric configuration were formulated by Sakharov in 1967 [2] and they include:

1. **Violation of baryon number $\boldsymbol{B}$**. The baryon number is defined as $B = n_b - n_{\bar{b}}$. There must be elementary processes that violate baryon number such that baryogenesis can proceed from an initial $B = 0$ to a universe with $B > 0$.

2. **Violation of $\boldsymbol{C}$ and $\boldsymbol{CP}$ symmetries**. It is demonstrated that if the charge conjugation symmetry C and the combined symmetry CP were exact, then the reactions that generate an excess of baryons would occur at the same rate as the conjugate reactions that generate an excess of antibaryons. Thus, the baryon asymmetry would retain its initial value $\eta = 0$.

3. **Departure from thermal equilibrium**. Baryon asymmetry generating processes must take place far from thermal equilibrium. If this was not the case, particle production reactions and their inverses would have the same rate and there would be no net increase in the number of particles.

Remarkably, over the years it was realized that the Standard Model (SM) does contain all three ingredients. Despite that, the predicted baryon asymmetry falls orders of magnitude short of the baryon asymmetry that is observed experimentally. In particular, the SM contributions to CP violation are too small to explain baryogenesis.

1.2 CP violation in the SM and beyond

In the standard model, treating neutrinos as massless, there are two sources of CP violation: one is the phase δ in the quark mixing matrix and the other is the θ_{QCD} coefficient.

The discovery and exploration of CP violation in the neutral B meson system [3] is, along with the existing data from CP violation observed with

K-mesons [4], in accord with the minimal model of CP violation known as the Kobayashi-Maskawa (KM) mechanism. This introduces the 3×3 unitary matrix V for three quark families (called the CKM mixing matrix) which defines the strength of flavor changing weak decays. Indeed, $|V_{ij}|^2$ is the probability that a quark of i flavor decays into a quark of j flavor. V involves three mixing angles and one CP violating phase δ. The smallness of CP violation is not because δ is small. This phase can be large, but the observed effects are strongly suppressed by small mixing angles. While the CKM matrix allows for CP violation in the quark-W boson coupling, it does not explain all of the observed CP asymmetry needed for baryogenesis. That is, the level of observed asymmetry between matter and antimatter in the universe is not explained by the Standard Model.

In quantum chromodynamics (QCD), CP violation comes from the so-called θ term, an additional gauge kinetic term of the Lagrangian. If its coefficient θ_{QCD} is nonzero, the violation of both P and T (or CP assuming the CPT theorem) symmetries occurs. Moreover, if θ_{QCD} were $O(1)$, one would predict a neutron EDM of sufficient size to ensure that the first EDM experiment of Purcell and Ramsey [5] would have detected it. In fact θ_{QCD} is now known to be tuned to zero, or at least to cancel, to better than one part in 10^{10}. This tuning is the well known *strong CP problem* of the Standard Model. In other words the strong interactions preserve CP to high degree of precision. It is not known wether θ_{QCD} is small due to an accidental cancellation or to some dynamical mechanisms. The most popular explanation is the existence of a new symmetry of QCD, called Peccei-Quinn symmetry [6], such that θ_{QCD} becomes a dynamical variable. The spontaneous breaking of the symmetry leads to a very light boson called the axion.

The standard model is not a complete theory [7] because it does not explain the particle-antiparticle asymmetry in the universe nor solve the hierarchy problem - why the masses of the known particles are so much smaller than the fundamental Plank mass (10^{19} GeV/c) or the grand-unification mass (10^{16} GeV/c). And it does not incorporate gravity. One of the most plausible extensions of the standard model is SuperSymmetry (SUSY), a symmetry between bosons and fermions. It adds new sources of CP violation but it doubles the number of particles. Each particle of the standard model has a more massive superpartner, so for example the photon's superpartner is the photino and the electron's is the selectron. Spin-zero bosons like the selectron can engage in CP violating interactions with electrons and quarks. Since the new interactions introduced by SUSY can provide a measurable electric dipole moment of fundamental particles, the EDM can

Figure 1.1: A particle with an EDM $\vec{d}$ parallel to its spin $\vec{\mu}$ is shown on the left side. An inversion through the origin, parity (P) reverses the EDM sign and leaves the spin direction unchanged. A time reversal operation T transforms the original particle into one with the same EDM but opposite spin direction. A rotation of 180° illustates that the particles depicted on right side are the same and unlike the particle on the left. Thus, violation of P and T can be seen as changing a particle with an EDM parallel to the spin direction into one whose EDM direction is antiparallel.

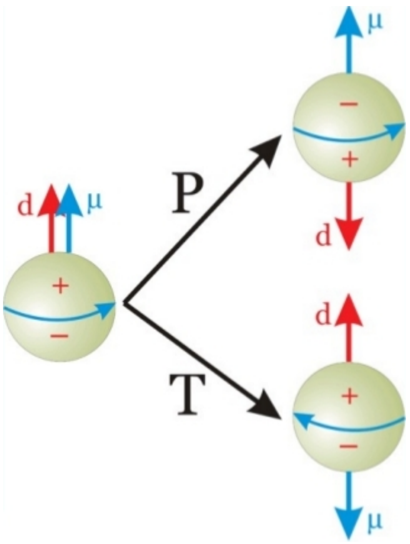

be a probe of new physics, as is explained in the following section.

1.3 The EDM as probe of new physics

As mentioned in the previous sections, time reversal and CP violation are closely related, in the sense that any CPT invariant interaction that violates one must violate the other. Nevertheless, CP and T are different symmetries with different physical consequences, so possible T violating observables open a new window on standard model tests and new physics searches. In particular, the effects of true CP violation are essentially limited to flavor changing processes such as K and B decays, while T odd observables such as electric dipole moment are also relevant for flavor diagonal channels.

The EDM of a fundamental particle is a charge displacement within the particle volume. It necessarily lies along its spin axis, because all components perpendicular to that average to zero. The alignment of spin and the EDM leads to violation of time reversal T, that inverts the time coordinate $t \to -t$, and parity P, that inverts the spatial coordinates $\vec{r} \to -\vec{r}$. As shown in Fig. 1.1, reversing time would reverse the spin direction but leave the EDM direction unchanged. So the existence of an EDM would be a violation of T. A parity operation would leave particle's spin unchanged but reverse the EDM sign, violating the P symmetry. Assuming the validity of the CPT theorem, violation of T implies a violaton of CP symmetry.

The idea to use the electric dipole moments of particles as a high-precision probe of symmetry properties of the strong interactions is due to Purcell and Ramsey in 1951. Remarkably, it precedes not only the discovery of CP violation in K mesons but also the discovery of parity violation in weak interactions. It was only 25 years later that the establishment of QCD as the theory of strong interactions led to the possibility of P and CP violation by the θ term. Although EDMs are not the only observables sensitive to non-CKM sources of CP violation, the remarkable degree of precision to which they can currently be measured endows them with a privileged status.

1.3.1 Theoretical predictions

The predicted EDM effects due to CKM mixing in the standard model are extremely small. The quark EDMs are only generated at the three-loop level and are expected to be [10]:

$$d_q^{CKM} \simeq 10^{-34} e\, cm \tag{1.2}$$

while the electron EDM only receives contributions from four-loop diagrams (at least for massless neutrinos) and should be:

$$d_e^{CKM} \leq 10^{-38} e\, cm. \tag{1.3}$$

The contributions to the neutron and proton EDM from the θ_{QCD} term in the QCD lagrangian is [11]:

$$|d_n^\theta| = |d_p^\theta| \simeq 4.5 \times 10^{-15} \theta_{QCD} \tag{1.4}$$

while the deuteron EDM is expected to be zero. In fact, the upper limit on d_n (see Sec. 1.3.2) now sets the upper limit on θ_{QCD} at $\leq 10^{-11}$.

Another scenario comes from SUSY where there are two contributions to CP violation: one from the quark-EDM (d_{up} and d_{down}) and the other from the chromo-EDM (d^c_{up} and d^c_{down}) where the EDM is generated in a loop containing a supersymmetric particle. Defining

$$\Delta = d_{down} - d_{up}/4, \quad \Delta^+ = d^c_{up} + d^c_{down}, \quad \Delta^- = d^c_{up} - d^c_{down},$$

neutron, proton and deuteron EDMs [12] are given by:

$$\begin{aligned} d_n &= 1.4\Delta + 0.83\Delta^+ - 0.27\Delta^- & (1.5)\\ d_p &= 1.4\Delta + 0.83\Delta^+ + 0.27\Delta^- & (1.6)\\ d_d &= d_{up} + d_{down} - 0.2\Delta^+ - 6\Delta^-. & (1.7) \end{aligned}$$

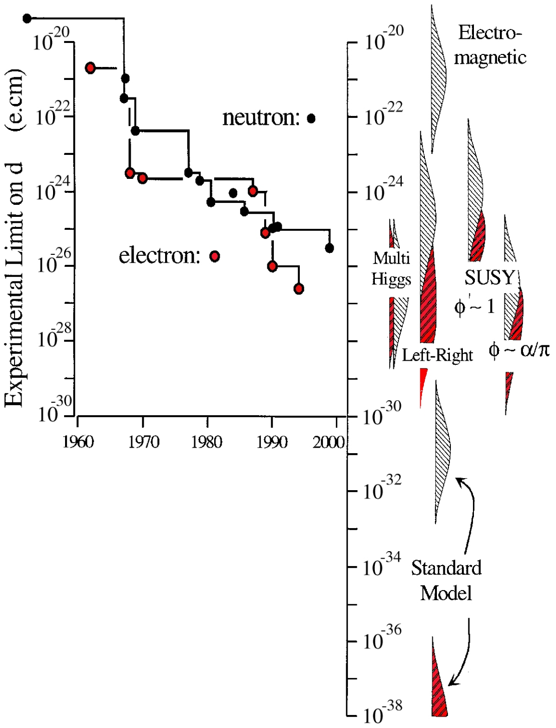

Figure 1.2: The experimental limits reached for neutron (black) and electron (red) EDMs are shown on the left side. On the right side there are the theoretical predictions of the standard model (the smallest values) and beyond, such as Multi Higgs, Left-Right, and SUSY models. Although no EDM has been measured yet, a discovery of a non-zero EDM between the current experimental bounds and the standard model calculations would be a signal of new physics [8].

If a non-zero deuteron EDM is measured, it would have a special sensitivity to the chromo-EDM due to the large coefficient of Δ^- in Eq. 1.7.

Because the *SM* contributions are expected to be small, EDMs are an excellent place to search for the effects of new physics. In Fig. 1.2 a comparison between experimental limits and the wide scenarios of theoretical expectations from the SM and beyond are shown.

No EDM of a fundamental particle has been measured yet. But if a non-zero EDM value is found between the actual experimental limits and standard model predictons it will be a clear signal of new physics and thus it will point to a new CP violation source.

1.3.2 Experiments

After the first experiment in 1951, the EDM search intensified and the level of experimental precision has improved steadily ever since. Indeed, following significant progress throughout the past decade, the EDMs of the neutron and several heavy atoms and molecules have been found to vanish to remarkably high precision.

In these measurements, the basic idea for detecting an EDM is to apply an electric field and look for the energy shift $-\vec{d} \cdot \vec{E}$. In most of the EDM experiments there is an external magnetic field $\vec{B}$ parallel to $\vec{E}$. Considering a particle of spin 1/2, the energy difference between magnetic and electric fields parallel or antiparallel is given by:

$$h\nu = 2\mu B \pm 2dE, \tag{1.8}$$

where h is Plank's constant, ν is the spin precession frequency, μ is the magnetic dipole moment and the ambiguous sign is determined by whether d and μ are parallel or antiparallel to each other. The tiny EDM effect is extracted by switching the polarity on the plates generating the electric field, thus reversing the sign of $\vec{E}$ relative to $\vec{B}$. Subtracting the measured frequencies cancels out the magnetic term and the EDM is given by:

$$d = \frac{h\Delta\nu}{4E} \tag{1.9}$$

Some results in the last decade are:

- $|d_e| \leq 1.6 \times 10^{-27}\mathrm{e} \cdot \mathrm{cm}$, the electron EDM limit derived from ^{205}Tl, a paramagnetic atom [13].
- $|d_n|_{exp} \leq 2.9 \times 10^{-26}\mathrm{e} \cdot \mathrm{cm}$, the neutron EDM limit measured on ultra cold neutrons [14].
- $|d_{atom}|_{exp} \leq 3.1 \times 10^{-29}\mathrm{e} \cdot \mathrm{cm}$, the atomic EDM limit measured on ^{199}Hg, a diamagnetic atoms from which an upper limit on the proton EDM has been derived ($|d_p| \leq 7.9 \times 10^{-25}\mathrm{e} \cdot \mathrm{cm}$) [15].

The atomic EDMs are complementary to those of the electron and neutron because they receive contributions not only from the EDMs of their constituents but also from CP violating eN or πN interactions (where N stands for a nucleon). Future experiments may improve the sensitivity significantly, by as much as four orders of magntude for d_e.

There are also prospects for new or greatly improved sensitivities to other EDMs, such as the muon, proton and deuteron. In these cases, the basic idea described for neutral systems does not work, since charged particles would be lost in an electric field. A new technique has to be developed and a plausible solution is a storage ring. For example, a proton or deuteron beam can be kept circulating in a storage ring with the polarization aligned along the momentum. The EDM signal would then arise from the interaction of the spin particles with a radial electric field (see Sec. 1.4). A proposal for the proton EDM experiment has been submitted with a sensitivity of $10^{-29} e\,cm$. To roughly estimate the scale of new physics probed by p/d EDM experiments, the EDM can be expressed on dimensional grounds as:

$$d_i \approx \frac{m_i}{\Lambda^2} e \sin\phi \tag{1.10}$$

where m_i is the quark or lepton mass, $\sin\phi$ is the result of CP violating phases, and Λ is the new physics mass or energy scale. For $m_q \sim 10$ MeV and $\sin\phi$ of order 1/2, one finds

$$|d_p| \sim |d_d| \sim 10^{-24} \left(\frac{1\text{TeV}}{\Lambda}\right)^2 e\,cm \tag{1.11}$$

Thus, for a d_p or $d_d \sim 10^{-29} e\,cm$ the sensitivity probe would be $\Lambda \sim 300$ TeV, a scale which is well beyond the center of mass energy of the LHC. Considering SUSY with superpartner masses $M_{SUSY} \leq 1$ TeV, if a d_p or $d_D \sim 10^{-29} e\,cm$ were not observed, $\sin\phi$ would be very small, $\leq 10^{-5}$.

No EDM has been found, but the current experiments set important constraints on the theoretical models. It is critical to carry out EDM experiments on different particles in order to understand where the source of CP violation originates.

1.4 EDM search in storage rings

As mentioned in the previous section, the new proposal to measure the EDM of a charged particle is based on the employment of a storage ring, a type of accelerator in which a particle beam can be kept circulating for a long period, up to hours.

Detection methods rest mainly on observing the precession of the polarization in an external electric field. Beginning with a longitudinally polarized beam in the storage ring, the EDM can be detected as a rotation of the polarization from the longitudinal to the vertical direction due to the interaction with the inward radial electric field that is always present in the particle frame (see Fig. 1.3(a)). This field, which bends the particle trajectories into a closed orbit, is present whether the ring is magnetic or electrostatic (as has been proposed for the proton case). However, it is first necessary to arrange the ring fields so that the precession of the spin relative to the velocity in the ring plane is suppressed. That precession (without the EDM component) is given by the Thomas-BMT equation [16] :

$$\vec{\omega}_G = \vec{\omega}_S - \vec{\omega}_C = -\frac{q}{m}\left\{G\vec{B} - \left[G - \left(\frac{m}{p}\right)^2\right]\frac{\vec{\beta}\times\vec{E}}{c}\right\} \tag{1.12}$$

where it is assumed that $\vec{\beta}\cdot\vec{B} = \vec{\beta}\cdot\vec{E} = 0$, and $\vec{\omega}_S$ is the spin precession in the horizontal plane, $\vec{\omega}_C$ is the particle angular frequency and $G = (g-2)/2$ is the particle anomalous magnetic moment (also denoted by a for leptonic anomalous moments). The spin precession can be frozen against the particle velocity with different methods, depending on the sign of the anomalous magnetic moment.

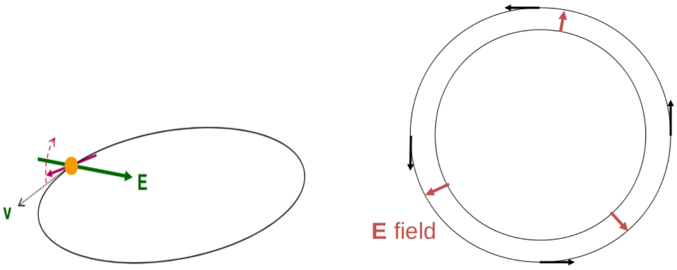

(a) (b)

Figure 1.3: The sketch in 1.3(a) shows the EDM signal of a charged particle in a storage ring. The purple arrow repesents the particle spin aligned along the velocity $\vec{v}$. Due to the EDM interaction with the inward electric field present in the particle frame, $\vec{E}$, the spin starts precessing in the vertical plane (orthogonal to the ring plane). The figure 1.3(b) shows in red the additional outward electric field needed for the deuteron EDM experiment to suppress the horizontal spin precession relative to the velocity.

For protons with $G = 1.79$, it is possible to make $\vec{\omega} = 0$ when $\vec{B} = 0$ (purely electrostatic bending elements) and $p = \frac{m}{\sqrt{G}} = 0.701$ GeV/c. This special value of the momentum is called the *magic momentum.*

For deuterons with $G = -0.14$, no such solution exists and the bending elements of the ring become a combination of vertical magnetic and outward radial electric fields such that the electric field is related to the magnetic field through

$$E = \frac{GBc\beta\gamma^2}{1 - G\beta^2\gamma^2}. \tag{1.13}$$

In both cases, ring and experiment performance are enhanced by choosing as large an electric field as is practical.

At EDM sensitivity levels approaching 10^{-29} e·cm, the EDM signal would be a precession on the order of 10^{-5} rad for a beam storage time of 20 min. It is crucial that during these 20 minutes that the beam polarization remains large for the EDM effect to accumulate to a measurable level. Normally, momentum spread among the beam particles leads to differences in the precession rates given in Eq. (1.12) and the particle spins will decohere by spreading in the horizontal plane. Thus, the aim of the next chapter is to analyze the contributions from the beam dynamics which can cause a horizontal polarization loss, preventing the EDM signal from being measurable. In particular, all the feasibility studies presented in this thesis are related to the deuteron EDM experiment. The conclusions, however, are general and apply to the proton case and any other storage ring EDM experiments.

Chapter 2

Elements of accelerator physics

The proposed method to measure the EDM of a charged particle requires the use of a storage ring. In this chapter, the main features of the beam dynamics in a storage ring will be described, including their effects on the beam polarization, as is shown in the measurements presented in the last two chapters. The topics illustrated here have been taken from Ref. [17].

2.1 Transverse beam dynamics

A particle beam can be kept circulating in a storage ring using dipole magnets, which bend the particle trajectory into a closed orbit. A stable transverse motion is guarateed by quadrupole magnets. In particular, quadrupoles provide linear restoring forces and it is often possible to treat the two transverse (vertical and radial directions) degrees of freedom as uncoupled.

2.1.1 Strong focusing

Strong focusing is a method based on alternating gradient field focusing, which makes use of quadrupole magnets. Since it is not possible to provide a restoring force in both transverse directions simultaneously (from $\vec{\nabla}\times\vec{B}=0$), it is necessary to alternate magnets focusing in the vertical and horizontal directions.

Quadrupoles can be constructed from iron shaped with a hyperbolic

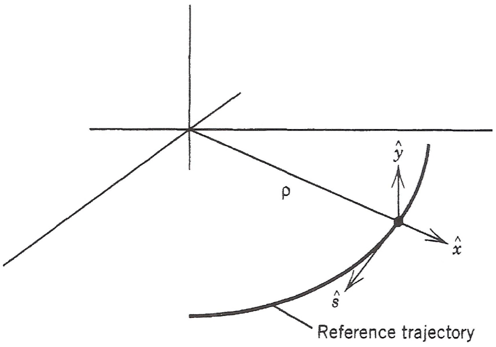

Figure 2.1: The new coordinate system for development of the transverse equations of motion.

profile. The resulting magnetic field is:

$$\vec{B} = B'(y\hat{x} + x\hat{y}), \tag{2.1}$$

where the field gradient $B' = \partial B_y/\partial x = \partial B_x/\partial y$ is evaluated at the center of the quadrupole and $\hat{x}, \hat{y}$ and $\hat{z}$ (shown as $\hat{s}$ in Fig. 2.1) are the unit vectors in the horizontal, vertical and longitudinal directions. For a charged particle passing through the center of a quadrupole, the magnetic field is zero. At a displacement (x,y) from the center, the Lorentz force on a particle with charge e and velocity v becomes:

$$\vec{F} = evB'\hat{z} \times (y\hat{x} + x\hat{y}) = evB'y\hat{y} - evB'x\hat{x}. \tag{2.2}$$

Thus, a focusing quadrupole in the horizontal direction ($\hat{x}$) is also a defocusing quadrupole in the vertical direction ($\hat{y}$) and vice versa.

2.1.2 Equation of motion

The description of transverse particle motion begins with a *closed orbit*, defined as the particle trajectory that closes on itself after one turn, and small amplitude oscillations around the closed orbit, called *betatron oscillations*. The closed orbit is defined by bending magnets (dipoles) which provide a path for a complete revolution of the particle beam. Since the bending angle of a dipole depends on the particle momentum ($B\rho = pe$), the resulting closed orbits will also depend on the particle momentum. Betatron motion around the closed orbit is determined by the arrangement of quadrupoles.

To properly write the equation of motion, a dedicated coordinate system is needed as is sketched in Fig. 2.1. Locally, the design trajectory (reference orbit) has a radius ρ and the path length along this curve is s. At any point along the reference orbit, three unit vectors can be defined: $\hat{s}, \hat{x}, \hat{y}$. The position of a particle is then expressed as a vector $\vec{R}$ in the form:

$$\vec{R} = r\hat{x} + y\hat{y}, \quad \text{where } r \equiv \rho + x. \tag{2.3}$$

Let's consider a generic particle with the correct momentum required for the experiment. This is called *reference* or *synchronous* particle. The coordinates defining its position and motion in the horizontal and vertical plane are respectively (x, x') and (y, y'), where $x' = dx/ds$ and $y' = dy/ds$ represent the divergences from the reference orbit. In general, the equations of motion will be non-linear. But assuming only linear fields in x and y (such as dipoles and quadrupoles) and keeping only the lowest order terms in x and y, the linearized betatron equation of motion is given by the Hill's equation:

$$\frac{d^2x}{ds^2} + \left[\frac{1}{\rho^2} + \frac{1}{B\rho}\frac{\partial B_y(s)}{\partial x}\right] x = 0 \tag{2.4}$$

$$\frac{d^2y}{ds^2} - \frac{1}{B\rho}\frac{\partial B_y(s)}{\partial x} y = 0. \tag{2.5}$$

Let (z, z') represent either horizontal and vertical phase space coordinates. The equations above are both of form $z'' + K_z(s)z = 0$, and differs form a simple harmonic oscillator only in the "spring constant" K_z, which is a function of position s. The general solution can be expressed in the form:

$$z = \sqrt{A\beta_z(s)} \cos[\psi_z(s) + \psi_z(0)] \tag{2.6}$$

where A and $\psi_z(0)$ are constants to be determined from the initial conditions and $\beta_z(s)$ is the *betatron amplitude function.* This is a pseudo-harmonic oscillation with varying amplitude $\beta_z(s)^{1/2}$ and the local betatron wavelength is $\lambda = 2\pi\beta_z(s)$.

The *phase advance* is given by:

$$\psi_z(0 \to s) \equiv \Delta\psi = \int_0^s \frac{1}{\beta_z(s)} ds, \tag{2.7}$$

and thus, for a circulare machine, the number of oscillations per turn is

$$Q_z \equiv \frac{1}{2\pi} \oint \frac{1}{\beta_z(s)} ds, \tag{2.8}$$

which is called *betatron tune* of the accelerator. If Q_z were an integer number, any errors in the magnetic fields of the magnets will be amplified since

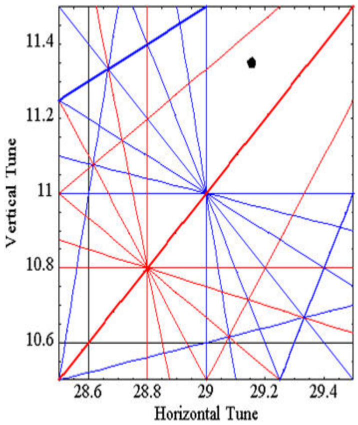

Figure 2.2: A resonance diagram for the Diamond light source. The lines shown are the resonances and the black dot shows a suitable place where the machine could be operated. Image courtesy *J.A. Clarke et al, STFC Daresbury Laboratory.*

the particle will be in exactly the same place each time it passes through the magnet, so this error will get amplified. These field errors cause the particle to take the wrong path and will eventually cause it to be lost. If the particle has an integer plus a half tune it will see this same error every second turn and integer plus a third will see the error every third turn and so on. Tunes in different planes can also combine to cause errors in the particle path. The places where these tunes and combinations of tunes occur are called resonances. They are referred to as first, second, third order etc. referring to integer, half integer, third integer fractional tunes etc. The lowest order resonances are the most problematic. Most particle accelerators do not have to worry about tunes beyond about fourth or fifth order since the oscillations are usually damped on a sufficiently short time scale that they are not a problem. A simple example is shown in Fig. 2.2 where the lines represent the resonances and a good working place is indicated by a black dot.

It is useful to define other two new variables[1]:

$$\alpha \equiv -\frac{1}{2}\frac{d\beta(s)}{ds} \tag{2.9}$$

$$\gamma \equiv \frac{1+\alpha^2}{\beta} \tag{2.10}$$

that together with $\beta(s)$ compose the *Courant-Snyder* or *Twiss parameters.*

---

[1] To simplify the notation, the subscript z is neglected hereafter.

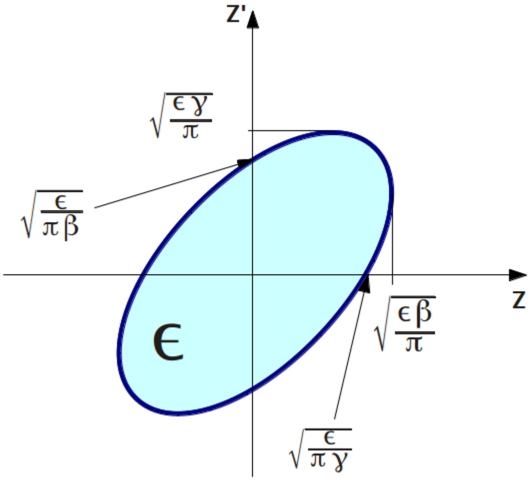

Figure 2.3: The Courant-Snyder invariant ellipse defined by α, β, γ. The area enclosed by the ellipse is equal to ϵ. The maximum amplitude of the betatron motion is $\sqrt{\frac{\epsilon\beta}{\pi}}$ and the maximum angle is $\sqrt{\frac{\epsilon\gamma}{\pi}}$.

Using the new notation, it is possible to rewrite the Hill's equation as:

$$A = \gamma z^2 + 2\alpha z z' + \beta z'^2 \tag{2.11}$$

where πA is the area of the Courant-Snyder invariant ellipse (see Fig. 2.3). The trajectory of particle motion with initial condition (z_0, z'_0) follows the ellipse described by the Eq. (2.11). The phase space area πA enclosed by (z, z') is constant at all places along the orbit while the shape of the ellipse evolves as the particle moves. After one turn, the ellipse returns to its orignal shape while the particle has propagated on the ellipse by a certain phase angle. The phase space area associated with the largest ellipse that the accelerator will accept is called the *admittance*. The phase space area occupied by the beam is called the *emittance*, $\epsilon = \pi A$, and commonly measured in $\pi \cdot \mathrm{mm} \cdot \mathrm{mrad}$. The maximum displacement z and angle z' at one point s along the orbit are given by:

$$z = \sqrt{\frac{\epsilon\beta(s)}{\pi}} \quad \text{and} \quad z' = \sqrt{\frac{\epsilon\gamma(s)}{\pi}}. \tag{2.12}$$

It is often convinient to speak of emittance for a particle distribution in terms of rms transverse beam size. Assuming a Gaussian particle distribution in both transverse degrees of freedom and an equilibrium situation where the distribution is indistinguishable from turn to turn, the emittance is given by:

$$\epsilon = -\frac{2\pi\sigma_z^2}{\beta(s)} \ln(1-F) \tag{2.13}$$

at a point s where the amplitude function is $\beta(s)$ and σ_z is the rms beam size. F represents the beam fraction included in the phase space area ϵ. Measuring the transverse beam width σ_z (for example with an Ionization Profile Monitor, IPM) the emittance can be calculated as:

$$\epsilon = \frac{\sigma_z^2}{\beta(s)} \tag{2.14}$$

2.1.3 Momentum dispersion

We have just examined the motion of particles having the same momentum as the ideal particle but differing in transverse position. What happens to a particle that differs in momentum by an amount $\Delta p = p - p_0$? As already mentioned before, the bending angle of a dipole depends on the particle momentum. Thus, the resulting closed orbits are displaced from the reference orbit by an amount defined by the *momentum dispersion function* $D(p, s)$. The displacement from the ideal trajectory of a particle due to the momentum spread is then given by:

$$x = D(p, s)\frac{\Delta p}{p_0} + x_\beta \tag{2.15}$$

where the first term represents the new closed orbit of the off-momentum particle and the second the betatron oscillation about that closed orbit.

In addition, higher momentum particles are bent less effectively in the focusing elements. That is, there is an effect analogous to chromatic aberration in conventional optics. The dependence of focusing on momentum will cause betatron oscillation tune dependence on momentum. The parameter quantifying this relationship is called *chromaticity* and it is defined as:

$$\delta\nu = \xi(p)\frac{\Delta p}{p_0}, \tag{2.16}$$

where $\delta\nu$ is the change in tune, $\xi(p)$ is the chromaticity and $\Delta p/p$ the fractional momentum deviation from the synchronous particle. The source of chromaticity discussed here is the dependece of focusing strength on momentum for ideal accelerator fields. This is called *natural chromaticity.* There are additional sources coming, for example, from field imperfections but they will not be treated here. It is important to worry about chromaticity because if the beam has a large momentum spread, then a large chromaticity may place some portion of the beam on resonance where it will be lost.

In order to correct the chromaticity effect, what is needed is a magnet that presents a gradient depending on the particle momentum. A distribution of sextupole magnets is normally used for this purpose. In the horizontal plane, the sextupole field is of the form

$$B = kx^2, \tag{2.17}$$

and so the field gradient on a displaced equilibrium orbit is

$$B' = 2kx = 2kD\frac{\Delta p}{p_0}. \tag{2.18}$$

Unfortunately, the sextupoles inevitably introduce non-linear aberrations which need a more complicated description than the linear dynamics briefly shown in this chapter.

Let's emphasize here the role of betatron oscillations on the particle path length. This is a crucial contribution to the horizontal polarization lifetime, as will be explained in the next chapter.

In general, a particle undergoing betatron oscillations travels a longer path compared to the ideal particle. Let's consider the simplest example in one dimension. Fig. 2.4 shows the reference orbit (horizontal straight line) and the trajectory of a particle undergoing a betatron oscillation by drawing a triangle built on the design orbit. The length of the segment along the hypotenuse is $L = L_0\sqrt{1+\theta^2}$, where θ is the angle deviation from the central ray. If the angle is small, the Taylor series expansion of the square root produces $\Delta L/L_0 = \theta_0^2/2$, but this is an overestimate. The velocity for the triangle path is a constant $v > v_0$. In fact, the velocity oscillates between these two extremes, remembering that this is added as a correction transverse to the main velocity around the ring. The best value then becomes the average of these two extremes, v and v_0, since the oscillation between them is sinusoidal. So there is another factor of 2 in the denominator. The X and Y contribution add in quadrature, so

$$\frac{\Delta L}{L_0} = \frac{\theta_x^2 + \theta_y^2}{4}. \tag{2.19}$$

Since bunching the beam (see Sec. 2.2) keeps all particles on average isochronous, such oscillations lead to a longer beam path and a higher particle speed, thus changing the spin tune. This concept describes a fundamental contribution to the horizontal polarization lifetime.

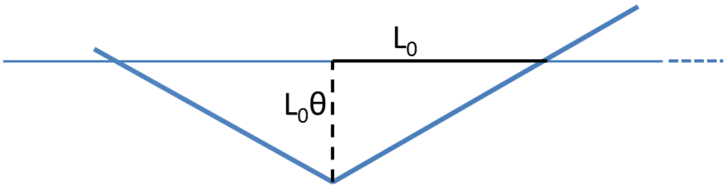

Figure 2.4: Sketch of a betatron oscillation in one dimension. The horizontal straight line represents the design orbit and is the basis of a triangle describing the particle trajectory undergoing a betatron oscillation.

2.2 Longitudinal beam dynamics

In a storage ring after the acceleration process to the experimental energy, the beam can be kept circulating in “packages” (*bunched beam*) or it can occupy the whole ring (*coasting beam*). In this section, the bunched beam case will be described since all the data presented in the thesis were taken under this condition.

The bunching process is obtained by using a radio-frequency (rf) cavity, which provides a longitudinal oscillating electric field. *Phase stability* ensures the stability of the longitudinal motion for particles in the bunch that normally differ in momentum from the ideal one.

2.2.1 Phase stability

For a particle with charge e, the energy gain per passage through the cavity gap is

$$\epsilon = eV_0 \sin(\omega_{rf} t + \phi_s), \tag{2.20}$$

where V_0 is the effective peak accelerating voltage, ω_{rf} is the rf frequency synchronized with the arrival time of the beam particles and ϕ_s is the phase angle. A particle synchronized with the rf phase $\phi = \phi_s$ at revolution period τ and momentum p_0 is called a *synchronous particle.* A synchronous particle will not gain/loose energy per passage through the rf cavity when $\phi_s = 0$. Normally the magnetic field is ideally arranged in such a way that the synchronous particle moves on a closed orbit that passes through the center of all magnets.

What happens to a particle with a slightly different momentum from the synchronous particle? Let L be the length of the ring circumference and v_0 the synchronous particle velocity. The time τ needed for one complete turn is given by $\tau = L/v$. The fractional change in τ associated with the deviation in L or v is:

$$\frac{\Delta\tau}{\tau} = \frac{\Delta L}{L} - \frac{\Delta v}{v_0}. \tag{2.21}$$

This means that a particle moving faster than the ideal particle will take less time to complete one turn. But if the path length is larger, this deviation will tend to increase the time to reach the rf cavity. The velocity deviation, can be expressed in terms of the fractional momentum deviation by

$$\frac{\Delta v}{v_0} = \frac{1}{\gamma^2}\left(\frac{\Delta p}{p_0}\right). \tag{2.22}$$

where γ is the relativistic factor. The orbit circumference can be larger for a particle of momentum slightly above the ideal particle momentum, since the magnetic rigidity ($B\rho = pe$) is proportional to the momentum. The fractional change in the orbit length for a given fractional change in the momentum is:

$$\frac{\Delta L}{L} = \alpha_c \frac{\Delta p}{p_0} \tag{2.23}$$

where α_c is the *momentum compaction factor*. Its value depends on the accelerator design. The fractional change in τ can finally be expressed in terms of $\Delta p/p_0$ as:

$$\frac{\Delta\tau}{\tau} = \left(\alpha_c - \frac{1}{\gamma^2}\right)\frac{\Delta p}{p_0} = \left(\frac{1}{\gamma_t^2} - \frac{1}{\gamma^2}\right)\frac{\Delta p}{p_0} = \eta\frac{\Delta p}{p_0} \tag{2.24}$$

where

$$\alpha_c \equiv \frac{1}{\gamma_t^2} \tag{2.25}$$

$$\eta = \frac{1}{\gamma_t^2} - \frac{1}{\gamma}. \tag{2.26}$$

γ_t is the *transition energy* and it is a property of the accelerator design, while η is the *slip factor*. Equivalently, Eq. (2.24) can be written in terms of the revolution frequency f_0 (the number of turns per second):

$$\frac{\Delta f}{f_0} = -\eta\frac{\Delta p}{p_0} \tag{2.27}$$

Eq. (2.27) is the key to understanding the concept of *phase stability*, as it is shown in Fig. 2.5. Below the transition energy, when $\eta < 0$, a higher energy particle ($\Delta p/p_0 > 0$) has a higher revolution frequency and it will arrive at the rf gap before the syncrhonous particle. That makes $\phi < 0$, the energy gain is $\epsilon < 0$, and the particle slows down. Similarly, a lower energy particle ($\Delta p/p_0 < 0$) will arrive at the rf cavity later and gain more energy relative to the synchrounous particle. This process provides the *phase stability* of synchrotron motion.

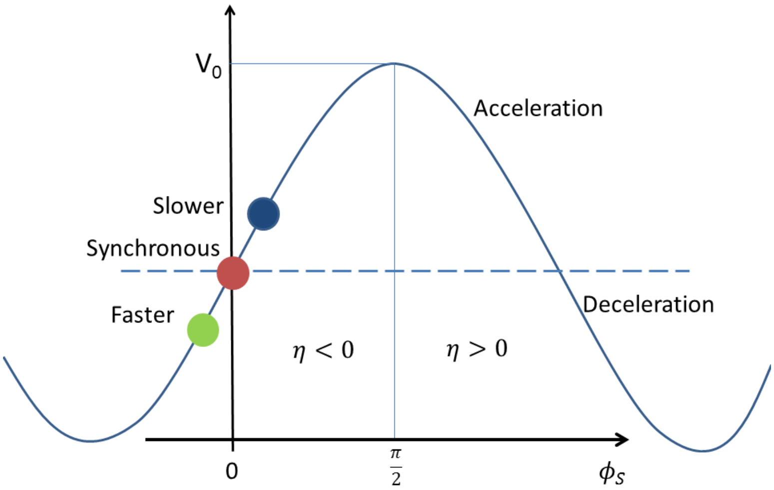

Figure 2.5: Schematic drawing of an rf wave, where the rf phase angles of a synchronous particle and the lower and higher energy particle are shown. For stationary motion, the phase stability requires $\phi_s = 0$ for $\eta < 0$ and $\phi_s = \pi$ for $\eta > 0$.

2.2.2 Equation of motion

From the phase stability process, the *synchrotron equations of motion* can be derived. They are two difference equations describing the motion of a particle with arbitrary energy E and phase ϕ with respect to the synchronous particle:

$$\phi_{n+1} = \phi_n + \frac{w_{rf}\tau\eta}{\beta^2 E_s}\Delta E_{n+1} \tag{2.28}$$

$$\Delta E_{n+1} = \Delta E_n + eV(\sin\phi_n - \sin\phi_s) \tag{2.29}$$

where the subscript n stands for the nth traversal of the rf cavity and $\Delta E = E - E_s$ represents the energy difference between a generic particle and the synchronous particle. $(\phi, \Delta E)$ are pairs of conjugate phase-space coordinates. The demonstration can be found in D. A. Edwards's and M. J. Syphers's book in Ref. [17].

In Fig (2.6) the application of the synchrotron equation of motion is shown for 8 different initial enegies (ΔE). In each case, the starting value of the phase is equal to the synchrotron phase. Several features are noteworthy. There is a well defined boundary between the confined and unconfined motion. This boundary is called the *separatrix*. The area in phase space within the separatrix is called a *bucket* while the collection of particles

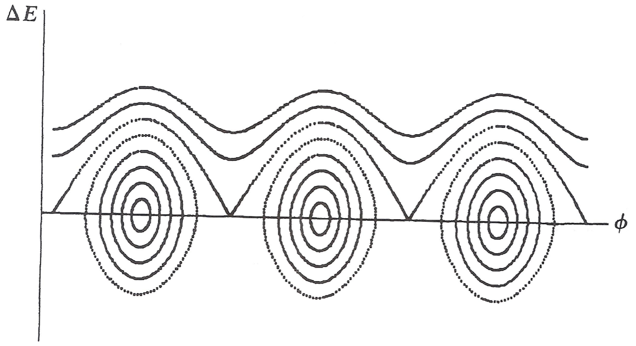

Figure 2.6: Application of the difference equations for synchrotron motion for a stationary condition (no acceleration). Each orbit represents a different initial condition. All of them start with the synchronous phase but different energies.

sharing a particular bucket is called a *bunch*. Finally, the *harmonic number* corresponds to the number of buckets.

The two difference equations, Eqs. (2.28) and (2.29), can be turned into one differential equation of the second order, assuming the turn number n as an independent variable. After a first integral and assuming $\Delta\phi = \phi - \phi_s$ being small, the equation becomes:

$$\frac{d^2\Delta\phi}{dn^2} + (2\pi\nu_s)^2\Delta\phi = 0 \tag{2.30}$$

where ν_s is the *synchrotron tune*, that is the number of synchrotron oscillations per turn. This quantity is given by:

$$\nu_s = \sqrt{-\frac{\omega_{rf}\tau eV\eta\cos\phi_s}{4\pi^2\beta^2E_s}}, \tag{2.31}$$

where $\eta\cos\phi_s < 0$ is the stability condition. The synchrotron oscillation frequency is $2\pi f\nu_s$, where f is the revolution frequency, and it is much smaller than the betatron oscillation frequency.

Chapter 3

The COSY storage ring

The COoler SYnchrotron COSY (see Fig. 3.1) at the Forschungszentrum-Jülich represents an ideal environment for the feasibility studies of the storage EDM experiment. For the experients described here, a deuteron beam was used.

It is a ring of 184 m length where two ion sources [18] provide polarized and unpolarized protons and deuterons. These beams are accelerated in the JULIC cyclotron and strip-injected into the COSY ring where they can be accelerated and used for the experiments in a momentum range from 300 MeV/c to 3.7 GeV/c. Electron cooling (electron energy 25-100 keV) at or near injection momentum and stochastic cooling covering the range from 1.5 GeV/c up to the maximum momentum are available to prepare monochromatic beams. The installation of vertical and horizontal dampers at COSY provides the possibility to stack electron-cooled beams and thus increase the beam intensity up to $\sim 10^{10}$ stored particles.

After the polarized source, the cyclotron accelerates the beam to the injection energy where the Low Energy Polarimeter (LEP) provides a polarization measurement of the states generated by the source. The rf solenoid (see Fig. 3.2) placed in one arc of COSY is a powerful tool to manipulate the beam polarization. Indeed, in the experiments presented in the next chapters, it was used to move the polarization from the vertical (stable) axis to the horizontal (ring) plane by inducing a spin resonance, whose features have been studied as a function of the emittance of the beam. Finally, the EDDA scintillator detectors (see Fig. 3.5) have been used as a mock EDM polarimeter to measure the vertical and the horizontal polarization components as a fuction of time, as is explained in the next section.

This chapter aims to describe the experimental setup and in particular the polarization measurements and the data acquisition systems used to record the data presented in this thesis.

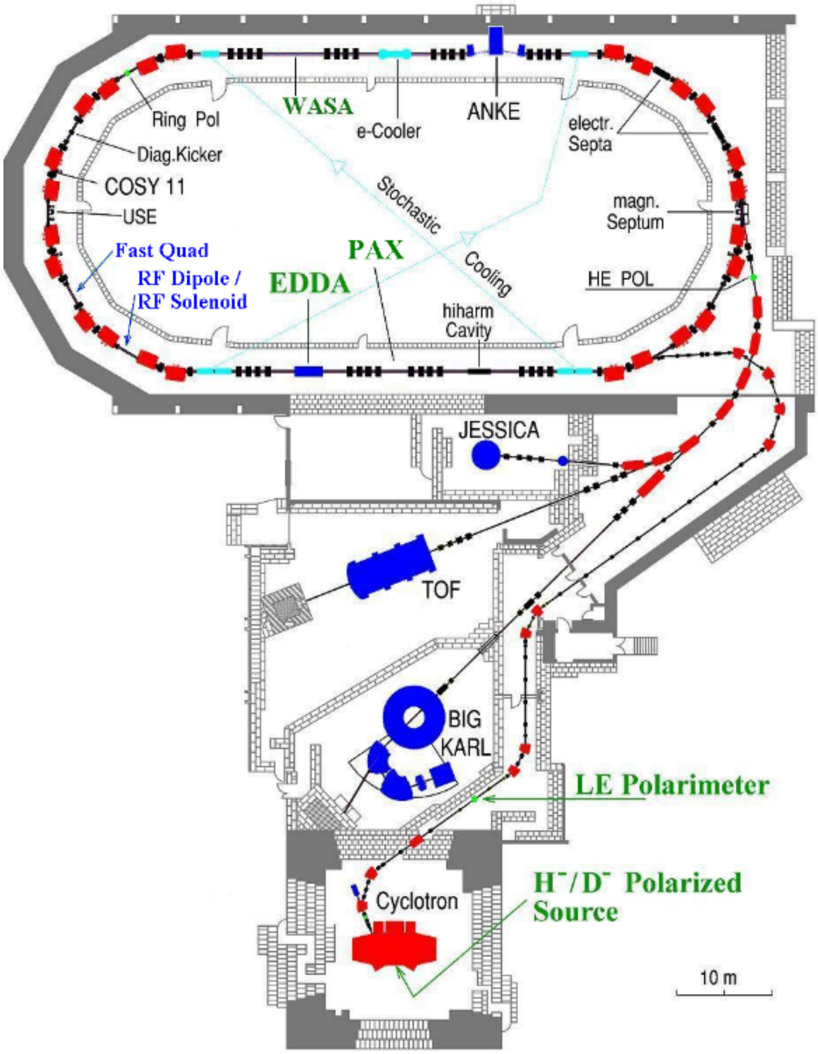

Figure 3.1: The COSY ring. Starting from the bottom: the beam sources providing polarized and unpolarized protons and deuterons, the cyclotron accelerating the beam to the injection energy, the low energy polarimeter (LEP) measuring the beam polarization, the COSY ring with the rf solenoid, and the EDDA polarimeter.

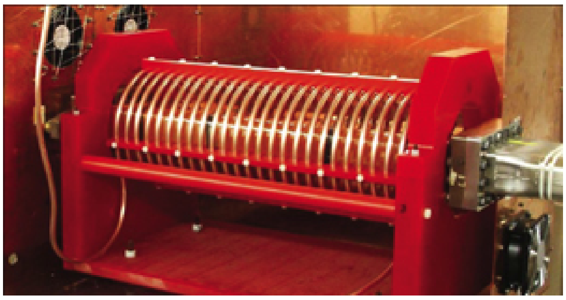

Figure 3.2: The rf solenoid used to manipulate the beam polarization.

3.1 Experimental techniques and setup

3.1.1 Polarization measurement

For a beam of particles, the *polarization* is defined as the ensemble average of the individual spins. In a spin-1 system [19] such as deuterons, there are three magnetic states along the quantization axis. In Cartesian notation, the fractional populations of the deuterons in terms of the magnetic quantum number along some spin axis is given by f_1, f_0 and f_{-1}, where $f_1 + f_0 + f_{-1} = 1$. The unpolarized state is described by the condition $f_1 = f_0 = f_{-1} = 1/3$, while the vector p_V and tensor p_T polarizations are defined by

$$p_V = f_1 - f_{-1} \quad \text{and} \quad p_T = 1 - 3f_0. \tag{3.1}$$

The range of the vector polarization p_V is from 1 to -1, while the range of the tensor polarization p_T is from 1 to -2. Given that the sum of the fractions has to remain 1, a pure vector polarization without tensor ($f_0 = 1/3$) can only reach $|p_V| = 2/3$. If a large tensor polarization is allowed, values may reach $|p_V| = 1$. These values may be reduced by any inefficiency in the polarized source operation.

The polarization of a deuteron beam can be determined by measuring deuteron-induced reaction rates on a target, provided that the relevant analyzing powers (or sensitivities to the polarization) are sufficiently large. For the EDM experiment, the large vector analyazing power available with suitably chosen targets make it preferable to concentrate on this polarization measurement rather than the tensor. Fig 3.3 shows the definition of the spin direction with respect to a coordinate system determined by the detected reaction products. The beam defines the positive $\hat{z}$ axis. The location of the particle detector, along with the beam axis, defines the scattering plane and the direction of the positive $\hat{x}$ axis. The scattering angle is β. In

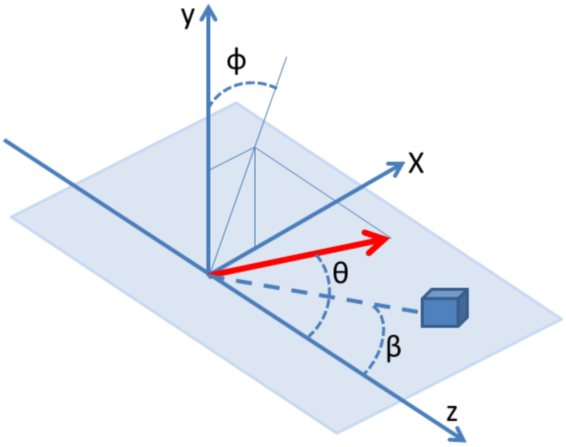

Figure 3.3: The coordinate system for polarization direction (red arrow) based on the observation of a reaction product in a detector (small box). The beam travels along the $\hat{z}$ axis. The detector position at angle β defines, along with the beam, the reaction plane and positive $\hat{x}$. The quantization axis for the polarization (red arrow) lies in a direction given by the polar angles θ and ϕ (as measured from $\hat{y}$ axis).

this coordinate system we can specify the orientation of the deuteron beam quantization axis by using the two angles of a spherical coordinate system, θ and ϕ, where ϕ is measured from the $\hat{y}$ axis and increases toward the positive $\hat{x}$ axis. The interaction cross section between a polarized deuteron beam and an unpolarized carbon target is given by:

$$\begin{aligned} \sigma(\beta,\theta,\phi) &= \sigma_{unp}(\beta)[1+\sqrt{3}\,p_V\,iT_{11}(\beta)\sin\theta\cos\phi \\ &+ \frac{1}{\sqrt{8}}\,p_T\,T_{20}(\beta)(3\cos^2\theta-1) \\ &- \sqrt{3}\,p_T\,T_{21}(\beta)\sin\theta\cos\theta\sin\phi \\ &- \frac{\sqrt{3}}{2}\,p_T\,T_{22}(\beta)\sin^2\theta\cos 2\phi] \end{aligned} \tag{3.2}$$

where the T_{kq} are the spherical tensor analyzing powers ($k = 1$ for vector, $k = 2$ for tensor). Both the unpolarized cross section and the analyzing powers are properties of the reaction.

Measurement of vertical polarization The reaction is most sensitive to the vertical (along $\hat{y}$ axis) component of the vector polarization when $\sin\theta\cos\phi$ is near 1 or -1. If both p_V and iT_{11} are positive, for example, then the rate at the detector (shown by the small box in Fig. 3.3) will increase relative to the unpolarized beam rate when $\sin\theta\cos\phi \sim 1$. Likewise, a detector on the opposite side of the beam (on the $-\hat{x}$ side) will see a reduced rate. The *asymmetry* in these two rates is a measure of the product $p_V\, iT_{11}$ and, for iT_{11} known, of the vertical component of p_V. If the left and right rates are L and R, then

$$\epsilon_{LR} = \sqrt{3}\, p_{V,y}\, iT_{11}(\beta) = \frac{L-R}{L+R}. \tag{3.3}$$

If positive $(+\hat{y})$ negative $(-\hat{y})$ vector polarization are available from the polarized source, the vector polarization can be determined from the *cross ratio* formula given by:

$$\epsilon_{CR} = \frac{r-1}{r+1} \quad \text{where} \quad r^2 = \frac{L(+)R(-)}{L(-)R(+)}, \tag{3.4}$$

and L and R are the count rates for the left and right systems for the positive $(+)$ and negative $(-)$ polarization states. Ths combinaion of count rates tends to suppress errors that arise as first-order contributions from geometric misalignments due to beam position or angle, or from detector acceptance.

Measurement of horizontal polarization If the polarization lies in the x-z plane or COSY ring plane, there will be a large and oscillating $\hat{x}$ component of the deuteron polarization due to the precession of the magnetic moment in the dipole fields in the ring. In a flat storage ring that is horizontal bending only, the stable spin direction is called *spin closed orbit*, $\hat{n}_{co}$, and coincides with the vertical axis, orthogonal to the ring plane. Any horizontal polarization component would precess about $\hat{n}_{co}$ while the beam circulates in the storage ring. In a similar manner as described above, this will generate a difference in count rates for detectors mounted above and below the beam, such that

$$\sqrt{3}\, p_{V,x}\, iT_{11}(\beta) = \epsilon_{DU} = \frac{D-U}{D+U}. \tag{3.5}$$

Spin tune This asymmetry will oscillate with the $g-2$ frequency. The number of spin precessions per turn about $\hat{n}_{co}$ is the *spin tune*, defined as:

$$\nu_s = G\gamma. \tag{3.6}$$

The spin precession rate depends on the particle velocity through the relativistic factor γ.

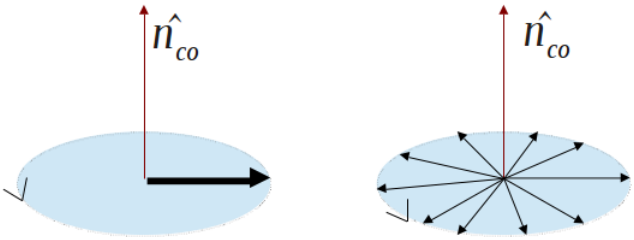

Figure 3.4: Starting from the left side, all the spins are alligned along the same direction so that the beam is horizontally polarized. After a while (right side), the spins spread out in the horizontal plane due to different particle velocities and thus different spin tunes. In this case, the horizontal polarization is lost.

Spin coherence time Let's consider a particle beam, polarized in one direction in the horizontal plane (see Fig. 3.4). After some time, the spins go out of phase due to the momentum spread of the particles in the beam, making the horizontal polarization vanish. For the purpose of this thesis, the horizontal polarization lifetime is the *spin coherence time*, the time during which the particle spins precess coherently around $\hat{n}_{co}$ while maintaining some fraction of their initial polarization. In an EDM experiment where the longitudinal polarization must be aligned along the velocity, the horizontal polarization lifetime represents the time available to measure the EDM signal.

3.1.2 EDDA polarimeter

One concept for the EDM polarimeter involves stopping detectors that deliver their largest signals for elastic scattering events, since they are the most sensitive to spin interactions. In order to reduce the background of other processes such as break-up interactions, an absorbing medium between the target and the detector is installed. This arrangement was already developed in a previous experiment [20] using a thick carbon target (see Fig. 3.5) and the scintillators of the EDDA detector [21]. Long scintillators, called "bars", run parallel to the beam and are read out with photomultiplier tubes mounted on the downstream end. These 32 scintillators are divided into groups of 8, corresponding to scattering to the left, right, down, or up directions. Outside the bars are "rings" that intercept particles scattering through a range of polar angles beginning at 9.1°. Four consecutive EDDA rings were included in the "polarimeter group", extending the sensitive angle range to 21.5°. Over this angle range, the vector analyzing power for the elastic scattering of deuterons from carbon is positive and passes through the

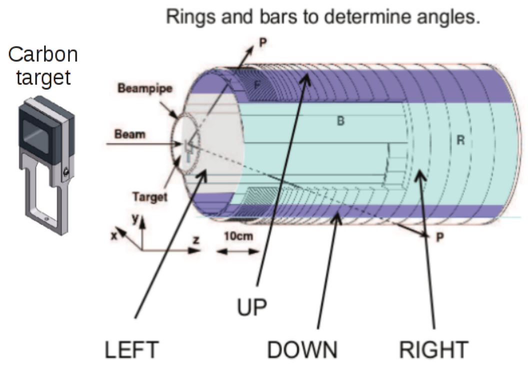

Figure 3.5: The carbon target used to extract the beam is placed in front of the EDDA detector. The left/right sectors are highlighted in light blue while up/down are in blue.

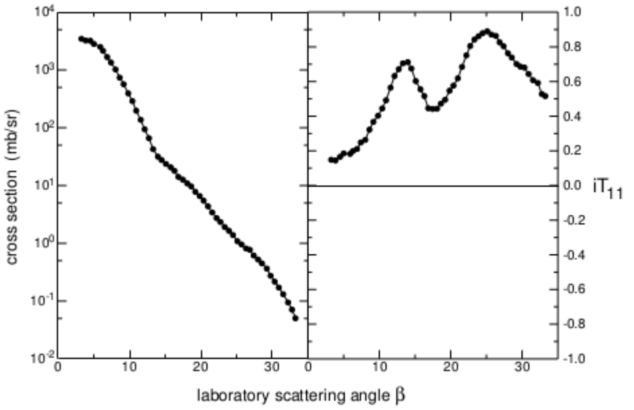

Figure 3.6: Deuteron elastic scattering cross section and vector analyzing power iT_{11} at 270 MeV [22].

first interference maximum [22] (see Fig. 3.6), making this an excellent range for operation as a polarimeter. The requirement that elastically scattered deuterons stop within the forward angle ring detectors led to the choice of 0.97 GeV/c as the optimum beam momentum.

Slow extraction In order to provide a continuous monitoring of the beam polarization during the storage time, the deuteron beam is slowly and continuously extracted onto a thick carbon target (see Fig. 3.5), a carbon tube 15 mm long that surrounds the beam [20]. Slow extraction of the beam onto the target is achieved by locally steering the beam vertically upward into the top edge of the tube. Deuterons intercepting the target front face pass through the full target thickness, which greatly increases their probability of scattering into the EDDA scintillator system. This polarimeter scheme offers a continuous monitor of the polarization during the beam store in contrast to previous experiments where observations were made at only one time during the polarization manipulation process [23].

3.2 Data Acquisition

3.2.1 Vertical polarization measurement

The triggers from the four segments (left, right, up, and down) of the EDDA detector were recorded in a single computer file for each run. A run consisted of a number of stores whose events could be added as a function of time since the start was synchronized to polarization precession operations through the use of a reproducible start time marker.

Analysis of the stores produced two cross ratio asymmetries, one for vector and one for vector-tensor polarized states. For comparison to the model calculations to be discussed later in Chap. 4, the two sets of cross ratio (see Eq. 3.4) data from each run were normalized to one based on the asymmetries recorded prior to any polarization manipulations being made. Then the two measurements were averaged. This combined all of the polarized beam data from a given run into one time-dependent set of vector polarization measurements.

3.2.2 Horizontal polarization measurement

The most critical new capability needed to measure the spin coherence time was the development of a “time-stamp system” which made possible recording the horizontal polarization as a function of time while it precessed at 120 kHz. Thanks to the efforts of E. J. Stephenson, who prepared the project, and V. Hejny, who wrote the DAQ software, the first direct measurement ever of the rapidly rotating horizontal polarization was accomplished.

A vertically polarized beam was injected into COSY and then the polarization was rotated to the horizontal plane (null vertical polarization) using the rf solenoid operating at the spin resonance:

$$f_{res} = f_{cyc}(1 - G\gamma) \tag{3.7}$$

where f_{cyc} is the cyclotron frequency and $G\gamma$ is the spin tune. The TDC, a ZEL GPX Time-to-Digital Converter (created locally at the Forschungs-

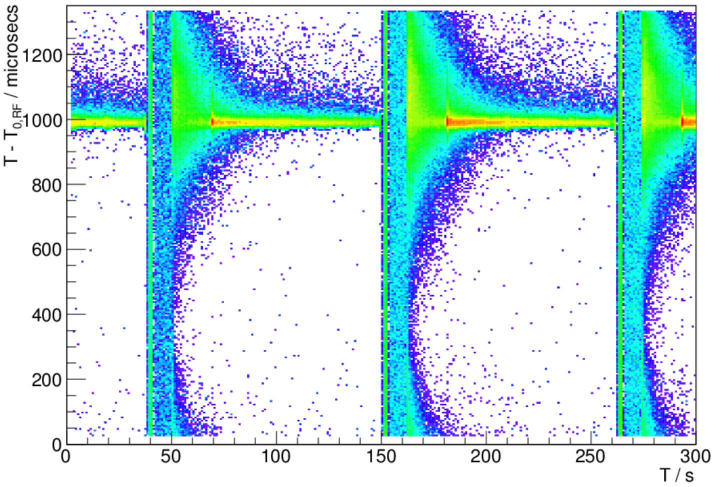

Figure 3.7: Scatterplot of polarimeter events as a function of location around the ring (vertical) and clock time in seconds (horizontal). There is sufficient time that parts of four different machine cycles are present. The intensity scale starts with violet and proceeds through blue, green, and yellow to red.

zentrum-Jülich) marked the polarimeter events with the elapsed time from a continuously running clock.

Particle position in the bunch The clock period of the TDC was 92.59 ps, a value much smaller than the COSY beam revolution time of 1.332 μs. This allowed good resolution on the longitudinal position of a detected particle within the beam bunch. Once the rf cavity signal and the TDC oscillator were cross-calibrated so that the turn number since DAQ start could be calculated, it became possible to use the fractional part of the turn number to provide a map of the particle distribution within the beam bunch. Fig. 3.7 is a scatterplot of polarimeter events as a function of location around the ring (vertical) and clock time in seconds (horizontal). It shows that as the cycles start, the beam is spread around the ring. The first few seconds are for injection, ramping, bunching, and the start of cooling. Bunching moves events out of the area near 300 and toward the center of the bunch near 1000 along the vertical axis. Electron cooling makes the bunch more compact (narrow yellow-red band). Outliers are slowly gathered into the main beam. After about 30 s, extraction of the bunch onto the polarimeter target starts. After that the height of the cooling peak declines until the beam is nearly gone. One machine cycle represents about 8.8×10^7 turns.

Total spin precession angle For the next step, calculating the total precession angle, only the integer part of the turn number is used. A phase factor may be used to locate the break point in Fig. 3.7 so that the turn number does not increment in the middle of the bunch. The calculation of the total precession angle requires the knowledge of the spin tune frequency, $G\gamma f_{cyc}$ (about 120 kHz). This value may be obtained from the difference between the rf solenoid resonance frequency and the cyclotron frequency (see Eq. 3.7). The rf solenoid spin resonance was determined at the beginning of the experiment using a variable-frequency Froissart-Stora [24] scan across the resonance (which flips the vertical polarization component) and refined with a series of fixed-frequency scans to locate the center of the resonance to within an error of about 0.2 Hz. With this as a start, the total horizontal polarization precession angle was calculated for each event as the product of the spin tune and the integral part of the turn number:

$$\omega_{TOT} = 2\pi\, G\gamma\, \mathrm{Int}(N_{turns}). \tag{3.8}$$

Amplitude of D/U asymmetry The circle around which the polarization precessed was divided into 9 bins and polarimeter events from the up and down detector quadrants sorted separately into each bin. The experimental challenge was the high frequency of the polarization precession. One full precession corresponded to only 6 turns of the COSY beam (about 8.3 μs) while the rate of the elastic scattered deuterons was approximately one in 700 turns. In order to provide some statistics, an accumulation time of 3 s was chosen and the down-up asymmetries were calculated for each bin and reproduced with a sine wave (see Fig. 3.8) of variable magnitude, phase, and offset (which is non-zero if there is a systematic difference in the detector acceptances):

$$\frac{D-U}{D+U} = f(\omega) = A\sin(\omega+\phi) + B. \tag{3.9}$$

The magnitudes from successive 3-second accumulation times were strung together to create a history of the horizontal polarization during the store. In the fitting of a sine curve to the down-up asymmetries, even a random distribution will produce a non-zero value of the amplitude. The so-called "positivity correction" of data will be described in Chap 5.

Spin tune refinement As a last refinement of the process, the spin tune itself was varied over a small range in each accumulation time to locate the value that gave the largest polarization magnitude. A peak was always

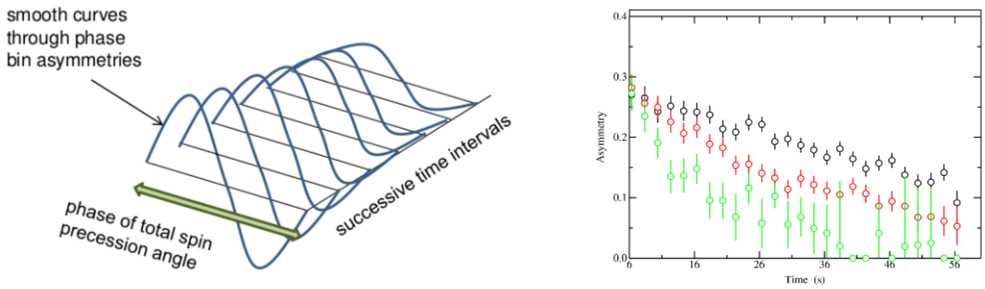

Figure 3.8: Sketch of the procedure to extract the horizontal polarization as a function of time from the total spin precession angle. On the left panel there are the sine waves, each of them used to fit a circle total spin precession angle accumulated for 3 s. On the right panel there is one example of the horizontal polarization measurement for three different beam emittances from a large (green) to a small (black) size. Each point of these curves corresponds to the amplitude of the sine wave, corrected for the "positivity" effect.

evident. Its FWHM was 1.8×10^{-6} of the value of the spin tune. Typically the spin tune would be known to 10^{-8} in each accumulation time and vary by 10^{-7} during a beam store. The variation appears to be associated with the changing spin tune across the profile of the beam as it is extracted onto the carbon polarimeter target.

Chapter 4

Study of an rf-solenoid spin resonance

The search for an electric dipole moment using a polarized, charged-particle beam in a storage ring requires ring conditions that can maintain a longitudinal and stable polarization for long time. In fact, the EDM signal would be detected as a vertical polarization component arising from the rotation of the horizontal plane polarization toward the vertical direction. For the deuteron case, the detection of the EDM signal at level above one part per million requires a horizontal polarization lifetime, also called the spin coeherence time, of at least 1000 s.

The spin coherence time depends on the spin tune spread of the particles in the beam. As explained in Chap. 3, the spin tune, which is the number of spin precessions around the vertical axis during one turn around the ring, is proportional to the particle velocity as expressed by the relativistic factor γ. In a real beam, particles have different velocities and spins will precess with different frequencies. For this reason, the initial horizontal polarization of the beam will vanish with time because the spins spread out in the horizontal plane.

The feasibility of the deuteron EDM experiment depends on the minimization of the spin tune spread. In order to understand the mechanism which causes it, a series of polarization studies began at COSY. The first step was the analysis of a spin resonance curve and the measurements are presented in this chapter. Since the width of a spin resonance curve depends on the spin tune spread and thus on particle momentum distribution, each meachanism that can change the particle velocity in the beam could contribute to the spin tune spread. In particular, these mechanisms are betatron oscillations which are due to the beam emittance and synchrotron oscillations that are present only in a bunched beam.

This study can be performed using either a coasting beam or a bunched beam.

In the first case, the particle beam is injected in the storage ring and it occupies the entire circumference. The main effect to the spin tune spread comes from $\Delta p/p$ (the fractional change in momentum respect to the reference particle) which kills the spin coherence time in milliseconds ($\sim (f_{cyc}\Delta p/p)^{-1}$). In this case there is no direct effect from the beam emittance on the momentum spread, since particles off from the reference orbit will undergo betatron oscillations simply covering a longer path compare to the reference particle.

For a bunched beam, the framework is completely different. An rf cavity confines the particles inside a bucket, as described in Chap. 2. Particles with a different velocity from the reference particle will undergo synchrotron oscillation inside the bunch such that the first order effect of $\Delta p/p$ averages to zero. The path lengthening due to betatron oscillations forces the particles to go faster in order to respect the isochronous condition introduced by the rf cavity. Thus, this effect can be described as a second order contribution from the beam emittance in the vertical and horizontal direction. A second order contribution from $\Delta p/p$ exists but is expected to be negligible compared to transverse size of the beam. The bunched case appears then to be a good solution in order to separately study the different contributions to the spin tune spread.

The tests at COSY made use of a bunched polarized deuteron beam with a momentum p=0.97 GeV/c. In order to provide a continuous measurement of the polarization as a function of time, the beam slowly extracted into a thick carbon target, placed in front of the EDDA detector. The vertical polarization was perturbed by a longitudinal radio-frequency (rf) magnetic field, inducing an rf depolarizing resonance which can flip the spin direction of stored polarized particles. The resonance frequency is defined as:

$$f_{res} = f_{cyc}(k \pm G\gamma) \tag{4.1}$$

where f_{cyc} is the cyclotron frequency and k is an integer. The studies began by exciting the $1 - G\gamma$ resonance and different tests were run at fixed and variable rf-solenoid frequency. Using a bunched beam, we compared the results obtained in case of electron-cooled and uncooled beam, since cooling shrinks the transverse sized of the beam and reduces the momentum spread $\Delta p/p$. The data analysis was based on a simple no-lattice model

Machine parameter	Value	
Tune, Q_x	3.60	
Tune, Q_y	3.62	
Compaction factor, α_c	0.177 ± 0.003	
Slip factor, η	-0.612 ± 0.003	
Beam parameters	**Uncooled**	**Cooled**
$\Delta p/p$	$(8.02 \pm 0.23) \cdot 10^{-4}$	$(4.91 \pm 0.13) \cdot 10^{-5}$
Width, ΔX	6.01 mm	1.43 mm
Width, ΔY	6.51 mm	1.77 mm
Emittance, ϵ_x	1.6 μm	0.09 μm
Emittance, ϵ_y	5.8 μm	0.42 μm

Table 4.1: Machine and beam parameters.

developed in order to reproduce the data collected during the beam time. The main focus of this analysis were the synchrotron oscillation effects on a spin resonance induced by an rf-solenoid, a side issue which may not help directly with the EDM study. The measurements presented in this chapter have been published for general accelerator physics in Ref.[25].

4.1 Machine parameters and measurements

The experimental set up used for beam extraction and polarization measurements has been described in Chap. 3. In order to have information available for modeling the results, a number of machine parameters were measured for the various running conditions. These are summarized in Table 4.1 where the slip factor η is calculated from the measure of α_c using Eq. 2.26 and the emittances are obtained by substituing the measured Gaussian beam widths (ΔX and ΔY) into the formula 2.14. The beam, with momentum $p = 0.97$ GeV/c, was bunched on the first harmonic ($h = 1$) with a maximum oscillator voltage of 400 V. For the uncooled beam, this captures most of the beam into about half of the ring circumference, as illustrated in Fig. 4.1. When electron cooling is applied at the beginning of beam storage, the momentum spread and the size of the beam are greatly reduced. The cyclotron frequency was 750602.5(5) Hz.

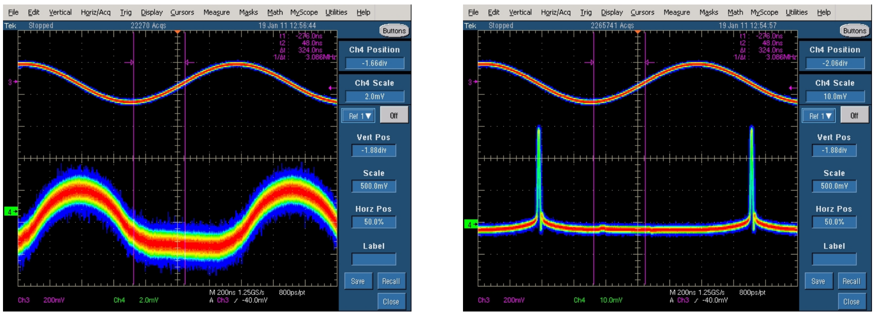

22270 Acqs 19 Jan 11 12:56:44
t1 : -276.0ns
t2 : 48.0ns
Δt : 324.0ns
1/Δt : 3.086MHz
Ch4 Position -1.66div
Ch4 Scale 2.0mV
Vert Pos -1.88div
Scale 500.0mV
Horz Pos 50.0%
Label
Ch3 200mV Ch4 2.0mV
M 200ns 1.25GS/s 800ps/pt
A Ch3 ⁄ -40.0mV

(a)

2265741 Acqs 19 Jan 11 12:54:57
t1 : -276.0ns
t2 : 48.0ns
Δt : 324.0ns
1/Δt : 3.086MHz
Ch4 Position -2.06div
Ch4 Scale 10.0mV
Vert Pos -1.88div
Scale 500.0mV
Horz Pos 50.0%
Label
Ch3 200mV Ch4 10.0mV
M 200ns 1.25GS/s 800ps/pt
A Ch3 ⁄ -40.0mV

(b)

Figure 4.1: Oscilloscope traces of the main rf (top) and beam pickup (bottom) for the **uncooled** (see Fig. 4.1(a)) and the **cooled** (see Fig. 4.1(b)) beam. The time trace represents roughly 1.5 rf periods. For the uncooled case, the pickup sees no beam for about half of the machine cycle, while in the cooled case the beam is gathered into a narrow bunch and there is a long residual uncooled tail on either side of pick.

Several measurements were made to study the dependence of the resonance width on the particle momentum distribution. The experiment started with a Froissart-Stora scan [24], ramping the solenoid frequency across the expected location of the resonance using an uncooled beam. The frequency at which the polarization changed sign was taken as the initial resonance location. It was then followed by a set of measurements at fixed solenoid frequency to compare the polarization oscillation patterns observed on and off-resonance for a cooled and an uncooled beam.

The next section will describe the model developed to analyze the data which includes two rotation matrices for the spin interaction with the magnetic fields of the ring and the rf-solenoid, and synchtron oscillations. The critical parameters for this model are the resonance frequency and the rf-solenoid strength, which are extracted from the comparison of the model with data as is shown in section 4.3. Then the full analysis of measurements presented here will follow.

4.2 Spin tracking model

The analysis of the data reported here is based on a "no lattice" model which I developed together with E. J. Stephenson. It is called the "no-lattice" model because it does not include explicitly the contribution of each magnetic device in the ring. Rather it describes the deuteron spin precession as simply due to two interactions of the spin with:

1. the vertical ($\hat{y}$ axis) magnetic field that arises from the cumulative effect of the ring dipoles.
2. the longitudinal ($\hat{z}$ axis) magnetic field of the rf solenoid.

These two effects are interpreted in a classical form using two rotation matrices which are applied to the spin particle on every turn around the ring.

The first rotation is around the $\hat{y}$ axis perpendicular to the ring plane. The precession angle on each turn is given by the size of the anomalous part of the deuteron magnetic moment, $G = (g-2)/2$:

$$\omega_a = 2\pi\nu_{\mathrm{S}} = 2\pi G\gamma \tag{4.2}$$

where $\nu_{\mathrm{S}} = G\gamma$ is the spin tune. The angle ω_a changes only as γ changes. The rotation matrix acting on the spin vector $\vec{S}$ becomes:

$$\vec{S'} = \begin{pmatrix} \cos\omega_a & 0 & -\sin\omega_a \\ 0 & 1 & 0 \\ \sin\omega_a & 0 & \cos\omega_a \end{pmatrix} \vec{S} \tag{4.3}$$

The second rotation is generated by an rf solenoid. It presents an oscillating field where the angle of spin rotation is given by

$$\theta_{\mathrm{S}} = 2\pi\epsilon\cos[2\pi f_{\mathrm{CYC}}(1-G\gamma)t + \delta(t) + \phi_{\mathrm{SOL}}] \tag{4.4}$$

where $t = n/f_{\mathrm{CYC}}$ with n the turn number and ϵ is the strength of the rf solenoid. The $1 - G\gamma$ harmonic of the spin tune $G\gamma$ was chosen before the experiment to best match the peak power output of the solenoid's driver amplifier. $\delta(t)$ represents a small perturbation that may or may not be time dependent and that is chosen in the design of the experiment to study phenomena near the resonance. Normally ϕ_{sol} is an arbitrary phase chosen in the interval $[0, 2\pi)$. The rf solenoid rotates the spin about the beam, or $\hat{z}$, direction. This rotation is described by

$$\vec{S'} = \begin{pmatrix} \cos\theta_{\mathrm{S}} & -\sin\theta_{\mathrm{S}} & 0 \\ \sin\theta_{\mathrm{S}} & \cos\theta_{\mathrm{S}} & 0 \\ 0 & 0 & 1 \end{pmatrix} \vec{S} \tag{4.5}$$

Repeated applications of these two rotations for each turn of the beam around the ring generates $\vec{S}(t)$ from a given starting point $\vec{S}(0)$.

This description is valid for the reference particle which travels along the design trajectory with the assigned momentum. Since the beam is bunched, the particles collected in the bucket undergo synchrotron oscillations whose contribution changes the particle velocity and the transit time through the solenoid. Synchrotron oscillations were added to the model as longitudinal sinusoidal oscillations in the z direction (along the beam) about the center of the beam bunch with amplitude A and a frequency $f_{\mathrm{SYNC}} = 331$ Hz as given by

$$z(t) = A\sin(2\pi f_{\mathrm{SYNC}} t + \phi_{\mathrm{SYNC}}) \tag{4.6}$$

At the same time there is an oscillation of the momentum whose change, $\Delta p/p$, is 90° out of phase with the position oscillation

$$\frac{\Delta p}{p}(t) = \frac{1}{\eta}\frac{f_{\mathrm{SYNC}}}{f_{\mathrm{CYC}}} 2\pi \frac{A}{C}\cos(2\pi f_{\mathrm{SYNC}} t + \phi_{\mathrm{SYNC}}) \tag{4.7}$$

where C is the ring circumference and η is the slip factor. Changes to the spin tune are scaled by

$$\frac{\Delta\nu_s}{\nu_s} = \beta^2\frac{\Delta p}{p} \tag{4.8}$$

The precession of the spin as it goes around the ring is changed because the momentum has changed, so that

$$\omega_a = 2\pi(\nu_s + \Delta\nu_S). \tag{4.9}$$

The main effect arises from transit time through the rf solenoid. Since particles have different velocities, they travel through it at different rf solenoid phases so that the rotation depends on the transit time:

$$\theta_{\mathrm{S}} = 2\pi\epsilon\cos\left(2\pi f_{\mathrm{CYC}}(1 - G\gamma)\left[t - \frac{A}{f_{\mathrm{CYC}}C}\sin(2\pi f_{\mathrm{SYNC}} t + \phi_{\mathrm{SYNC}})\right] + \delta(t) + \phi_{\mathrm{SOL}}\right). \tag{4.10}$$

Thus both the spin precession in the ring magnetic field and the effect of the rf-solenoid oscillate with the synchrotron motion of the particle. As will be covered in the next section, detailed agreement with the uncooled data was made possible by choosing the appropriate distribution of orbit amplitudes A.

The sine and cosine functions used here to describe the synchrotron motion represent the solution for the differential equation of simple harmonic motion in a parabolic potential. A more accurate model would involve a sinusoidal potential and numerical integration of the synchrotron motion. This was tested for the present situation. While this changes some details of the shape of the beam distributions described later, there is no essential change in either the quality of the reproduction of the measurements or the interpretation based on this model.

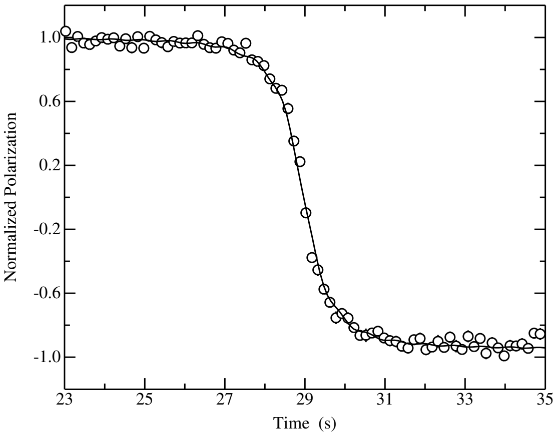

Figure 4.2: Froissart-Stora scan for the uncooled beam. The zero crossing was used to make a first estimate of the spin resonance frequency. The curve is calculated assuming a resonance frequency of 871434 Hz and a ramp rate of 10 Hz/s starting from 871200 Hz at 5.8 s. The calculation includes synchrotron oscillation effects as described in the text later.

4.3 Data analysis

4.3.1 Model parameters

The most important parameters of the "no lattice" model to reproduce the data are the resonance frequency $(1 - G\gamma)f_{\mathrm{CYC}}$ and the magnetic field strength ϵ of the rf solenoid.

The frequency of the $1 - G\gamma$ resonance was estimated at the beginning of the experiment by making a Froissart-Stora frequency sweep across the expected location of the resonance using the uncooled beam. The frequency at which the polarization changed sign was taken as the initial resonance location. Fig. 4.2 shows the data from this scan, which was started at 871200 Hz (at a time of 5.8 s) and ramped at a speed of 10 Hz/s for a total of 40 s. The zero crossing is clearly evident near 29 s and corresponds to 871434 Hz.

The solenoid strength was extracted by the interpretation of a cooled beam measurement on resonance, shown in Fig. 4.3. The data represent a slow oscillation of the vertical component of the polarization with a period of about 2/3 s. It persists for the 55 s that the rf solenoid was kept running after the initial ramp-up, which lasted 200 ms. This permits a very precise determination of the magnetic field strength of the rf solenoid by matching the frequency of the polarization oscillation using calculations with the model described in the previous section. The oscillation pattern requires an effective strength of $\epsilon = (4.05 \pm 0.01) \times 10^6$ rev/turn.

The knowledge of the resonance frequency can be improved using the rf solenoid operating at a fixed frequency in the immediate neighborhood of the resonance. Being off-resonance by even a fraction of one Hz creates clear changes in the polarization oscillation pattern. The most precise results were obtained with the cooled beam case in which the beam can be considered as “point-like” and the synchrotron oscillation contribution is very small (see Sec 4.3.2).

Four sets of data with a cooled and bunched beam were recorded with the rf solenoid frequency at ±1 and ±2 Hz from the nominal resonance frequency of 871434 Hz. Assuming that the rf solenoid strength was unchanged after the data taken in Fig. 4.3, then the only parameter that may be adjusted in order to match the oscillation frequency is the frequency separation between the rf solenoid and the resonance. The shifts needed for the off-resonance data are given in Table 4.1, along with the average and an error that spans the four cases of Fig. 4.4. Since the additional frequency shifts move the points below the resonance away from the resonance, and the points above the resonance toward the resonance, the resonance frequency is higher. The average shift gives a resonance position of 871434.13 ± 0.04 Hz. The error was estimated from the scatter in the shift measurements. The data and calculations of Fig. 4.4 illustrate the general features of the vertical polarization when operating the rf solenoid off-resonance. As the distance from the resonance increases,

- the oscillation frequency increases,
- the oscillation amplitude goes down,

as is shown in Fig. 4.4. Note in particular that the top of the oscillation pattern always remains close to one so that off-resonance polarization measurements quickly become completely positive.

In Fig. 4.4, the average polarization value of the calculated oscillation is more positive than the measurements, a trend that becomes more prominent as the distance from the resonance increases. The reason for this disagreement is not understood.

Once the resonant frequency and the frequency of the bunching cavity (750602.5 ± 0.5 Hz) are known, then it is possible to determine other parameters of the beam and the properties of the COSY ring for the setup that existed during this experiment. These are given in Table 4.3 where p

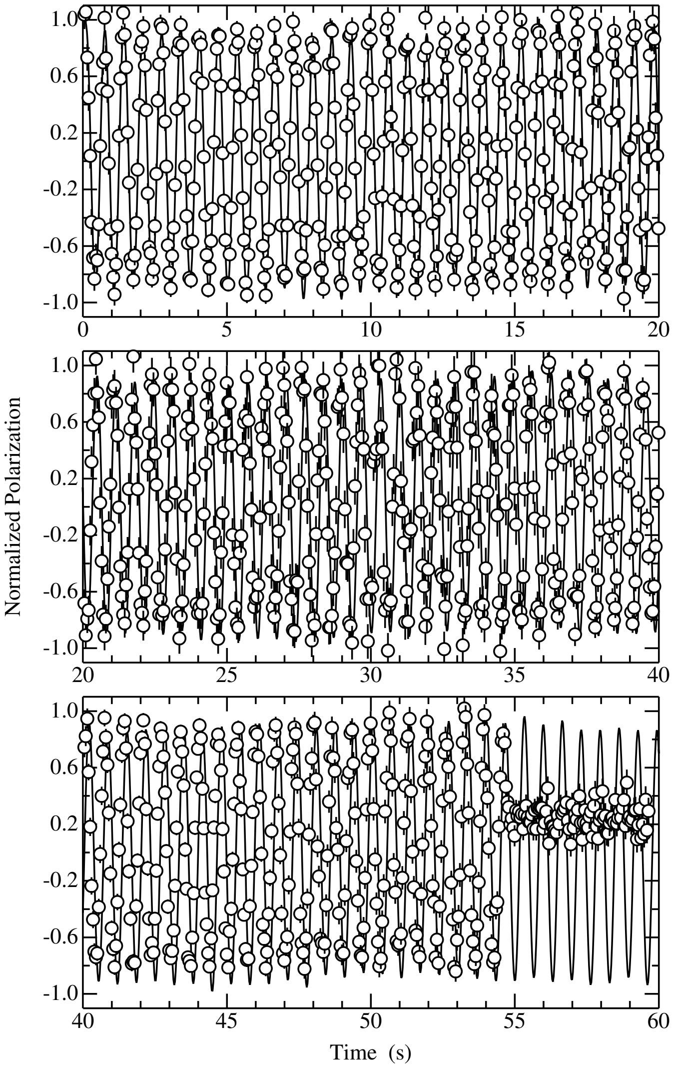

Figure 4.3: Cooled beam measurements on resonance. From this set of data where the vertical polarization oscillates for 55 s, it was possible to obtain a precise value for the solenoid field strength, $\epsilon = (4.05 \pm 0.01) \times 10^{-6}$ rev/turn. The empty circles are the data points recorded while the black line is the result of the “no lattice” model calculation.

Nominal shift (Hz)	Additional shift (Hz)	Osc. Freq. (Hz)
-2	-0.096	2.676
-1	-0.121	2.006
$+1$	-0.161	1.864
$+2$	-0.126	2.506
Average	-0.13 ± 0.04	

Table 4.2

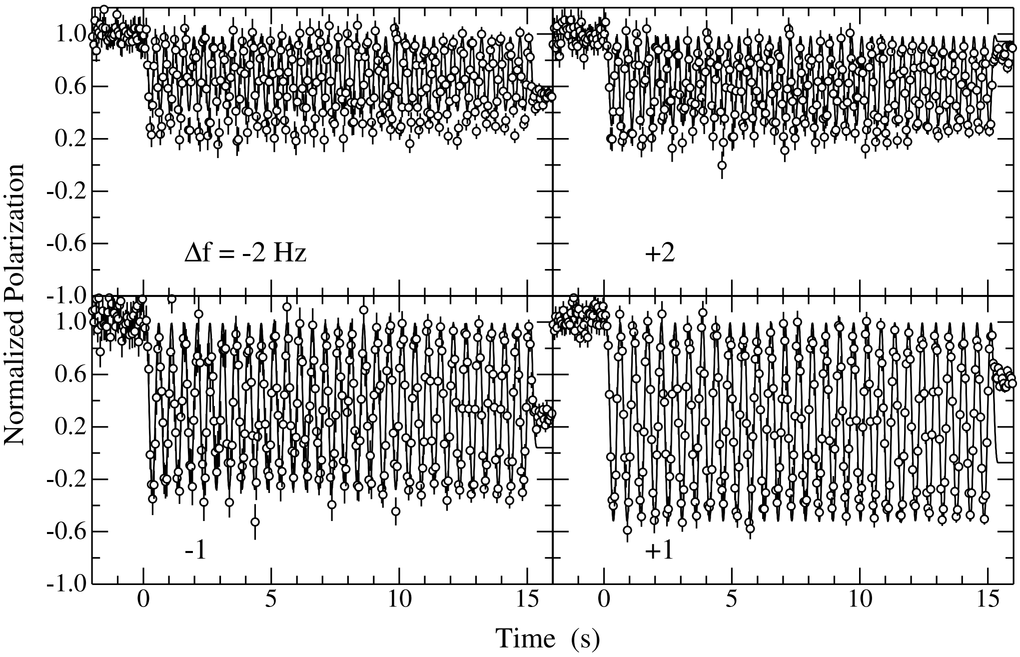

Figure 4.4: Fixed frequency measurements made off resonance at ±1 and ±2 Hz from the nominal value of 871434 Hz. By fitting the oscillation frequency of the data with the model calculations it was possible to refine the resonance frequency. The larger distance from the center of the resonance, the higher the frequency oscillation and the smaller the oscillation amplitude.

Assumed	c	299792458 m/s
	m_d	1875.612793(47) MeV/c^2
	G	$-0.14298754(26)$
Measured	f_{CYC}	750602.5(5) Hz
	f_{RES}	871434.13(4) Hz
	f_{SYNC}	331(1) Hz
Calculated	p	970.057(24) MeV/c
	C	183.4817(37) m
	T	236.006(11) MeV
	γ	1.1258289(58)
	β	0.4593905(89)

Table 4.3: Beam and machine parameters

is the beam momentum, C is the ring circumference, and T is the beam kinetic energy. All model calculations use these values.

4.3.2 Synchrotron oscillation effects

As already mentioned in Sec. 4.2, synchrotron oscillations change the transit time of the particle through the rf solenoid so that these particles do not feel the effect of the same magnetic field as the central particle. Such a time shift effect is enhanced when the rf solenoid operates on a harmonic of the deuteron spin tune, increasing its rate of change. In addition, when the rf cavity is operated on first harmonic, it allows a larger range of synchrotron oscillation amplitudes (the beam occupies half of the ring circumference).

Amplitude distribution Fig. 4.5 shows several tracks, each of them corresponding to a particle undergoing a synchrotron oscillation of amplitude A. With larger synchrotron amplitudes, the particle spends less time passing through the rf solenoid at times that are close to optimum for reversing the polarization. Thus this effectively weakens the solenoid and slows the oscillations for large values of A as appear in the figure. But still the polarization flips completely.

Unlike the continuous pattern of oscillations (see Fig. 4.3) measured with a cooled beam, the same experiment with an uncooled beam and

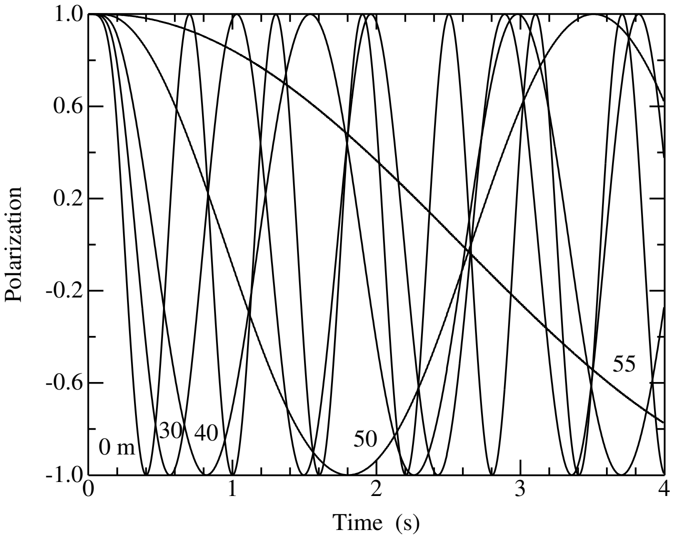

Figure 4.5: Single particle functions, $f_{A_i}(t)$ representing the change of the vertical polarization as a function of time for different synchrotron amplitudes, $A = 0, 30, 40, 50$ and 55 m. All these tracks are obtained from the model calculation on resonance. A clear effect of synchrotron oscillations is that the larger the amplitude, the longer the oscillation period.

large synchrotron amplitudes produces a pattern shown in Fig. 4.6 that is quickly damped. In order to model the oscillations of Fig. 4.6 (uncooled and bunched beam), it was necessary to find the correct amplitude distribution in the beam bunch. Aside from the distributions shown in Fig. 4.1, there is no direct knowledge from the experiment of the distribution of particles. It is possible to assume a Gaussian distribution, but this proves to be the wrong shape for a detailed reproduction of the measurements. The better choice was to fit the data with a function $P_y(t)$ given by the combination of single particle functions $f_A(t)$ for a specific amplitude A (like the curves shown in Fig. 4.5):

$$P_y(t) = c_1 f_{A_1}(t) + c_2 f_{A_2}(t) + \cdots + c_N f_{A_N}(t). \tag{4.11}$$

Representative values of A were chosen and the fitted fraction, c_i, of the tracks with different values of A that resulted is shown in Fig. 4.7(a). For further calculations, it seemed prudent to replace the fitted distribution of Fig. 4.7(a) with a larger number of tracks chosen randomly. Each point of Fig. 4.7(a) was replaced by a bin whose area represented the same fraction of the tracks and whose width was adjusted to span the range of Fig. 4.7(a). The 1000 random tracks were chosen with a distribution of amplitudes that matched the areas of the bins. In the case of the first bin with a negative

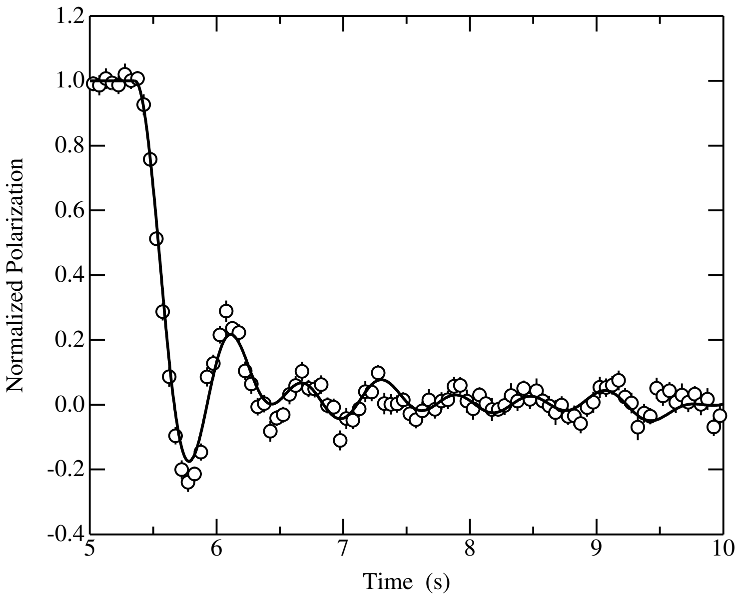

Figure 4.6: Measurements made on-resonance with the uncooled beam and an rf solenoid strength of 4.43×10^{-6} rev/turn.

coefficient, the sign was changed to a positive one to maintain the contribution of small amplitudes to the whole distribution. When this distribution is combined with random synchrotron phases, ϕ_{SYNC}, the resulting beam distribution is shown in Fig. 4.7(b). This shape compares favorably with Fig. 4.1(a).

Damped oscillations The contribution of synchrotron oscillations gives rise to damped oscillations which have characteristics different from off-resonant behavior. The damped oscillations are very sensitive to details of the synchrotron amplitude distribution. For example, in Fig. 4.8 there are two sets of measurements on-resonance for the uncooled beam, with two different solenoid strengths. The attempt to reproduce the data with same amplitude distribution used for the data in Fig. 4.6 partially failed.

This distribution of particles in the beam seems to change by small amounts over time during the experiment. Figs. 4.8(a) and 4.8(b) show time curves calculated with the model of Fig. 4.6, but with different solenoid strengths. In Fig. 4.8(b), agreement is not as good. In particular, more tracks are needed with small amplitudes and faster oscillation frequencies to better match the first two oscillations in the polarization. Adding such tracks improves the agreement for that feature, but this change overes-

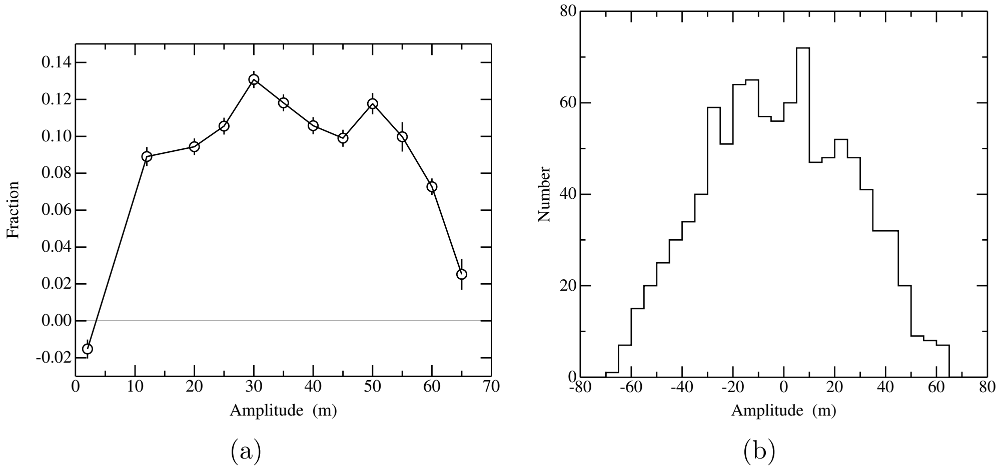

Figure 4.7: (a) Distribution of values of A leading to the model calculation of Fig. 4.6. Note that the first coefficient is negative, an unphysical result. (b) Distribution of particles in the beam obtained by reproducing the time dependence of Fig 4.6 with the amplitude distribution here on the left side and matching that with 1000 tracks following the same amplitude distribution.

timates the oscillations at larger times. The calculations shown in Figs. 4.8(a) and 4.8(b) are similar, but in Fig. 4.8(b) the data display different polarization oscillations and the central value is now positive. This supports the conclusion that the distribution of synchrotron amplitudes changes with time. It is possible to reproduce these measurements with a quality similar to that shown in Fig. 4.6 provided we repeat the fitting process and obtain a new set of coefficients similar to those in Fig. 4.7(a). During the several hours spent taking these measurements, it is likely that the distribution of particles within the rf bucket changed, even if the bucket potential is unchanged. These measurements are clearly very sensitive to that choice. The range of variation seen in Figs.4.8(a) and 4.8(b) demonstrate by example the level of stability of these features. Unfolding this through a fitting process produces a beam bunch distribution that is consistent with what is observed using beam pickup monitors.

Final polarization value from Froissart-Stora scan and the reflection point Due to the synchrotron oscillations, particles with particularly large amplitudes will respond to the rf solenoid as if it is effectively very weak. At some point these particles will no longer undergo a complete spin flip as the rf solenoid frequency passes over the position of the resonance. To illustrate this, a model calculation was made of the frequency scan of

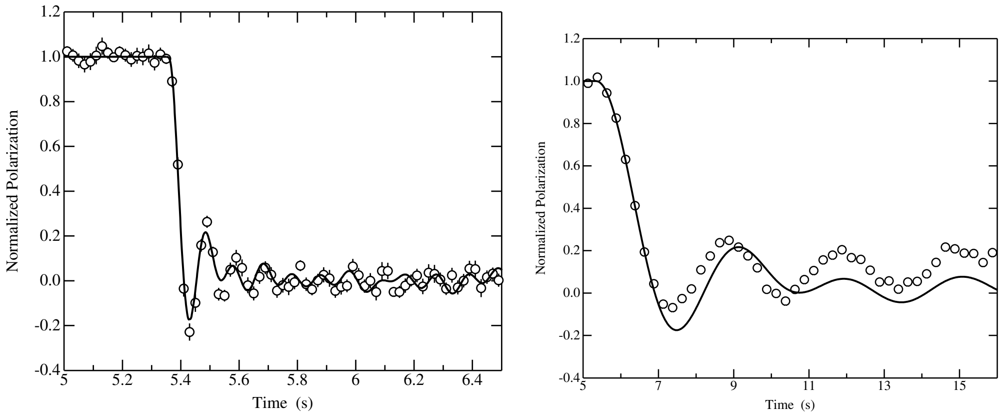

(a) (b)

Figure 4.8: (a) Measurements similar to Fig. 4.6 but with a solenoid strength of 2.66×10^{-5} rev/turn. The model calculation uses the distribution of 1000 randomly chosen amplitudes. (b) The same as Fig. 4.6 but with a solenoid strength of 8.87×10^{-7} rev/turn. The solenoid was turned off at $t = 15$ s.

Fig. 4.2 using the distribution of amplitudes shown in Fig. 4.7(b). Then, for each of the 1000 tracks in that simulation, the vertical projection of the spin was plotted at the end of the frequency scan. The result is shown in Fig. 4.9. For most of the range of amplitudes A, the final spin projection is practically indistinguishable from 1. At roughly $A = 48$ m, the effective solenoid strength becomes sufficiently weak that some departure can be seen from a final value of $p_Y = 1$. As the size of A increases, the result moves quickly to $+1$, and for higher values falls again toward -1. Some admixture of the large synchrotron amplitude particles into the beam bunch will thus cause the frequency scan to fall short of a complete polarization reversal. At the point near $A = 57.8$ m, where the final polarization goes to $+1$ the period of the oscillation in Fig.4.5 goes to infinity. For larger values of A the set of oscillating functions retraces its path back down again with progressively shorter and shorter polarization oscillation periods. Thus, $A = 57.8$ m is a reflection point in this pattern.

For the data in Fig. 4.2, the uncooled distribution of Fig. 4.7(b) resulted in a final polarization value of -0.8, while the measured value came close to -0.96. A closer reproduction required that the fraction of tracks in the region of $A > 50$ m be reduced by a factor of 5. This is another example of the change with time of the particle distribution in the bunch.

Another feature caused by synchrotron oscillations is that the polarization in Fig. 4.3 falls slightly short of reaching 1 or -1. When presented

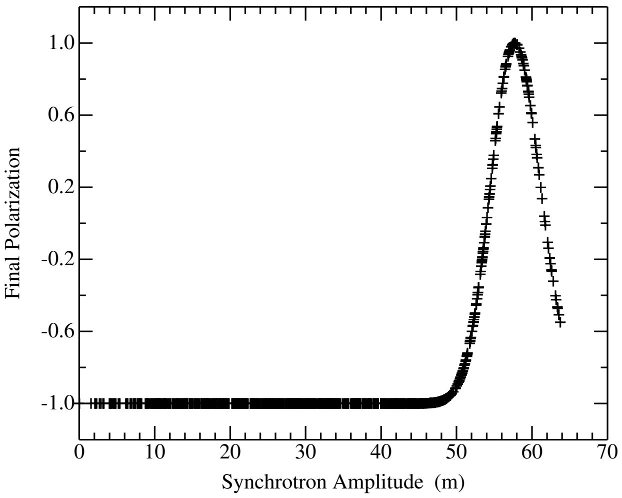

Figure 4.9: Final polarization value of a single particle track as a function of the synchrotron amplitude A after a frequency scan as shown in Fig. 4.2.

to a fitting program using the same basis set that was used for the uncooled beam, most of the strength appeared for amplitude that was closest to zero. The reminder, a few percent, was distributed widely among the larger amplitudes, as is shown in Fig. 4.10. The distribution in Fig. 4.10 compares well with the distribution measured by the beam pick up shown in Fig. 4.1(b), which also has tails emerging on each side of the central peak. In this case, the uncooled component is approximately 9%. This is probabily due to particle collisions with the residual gas in the beam pipe or close encounters with electrons in the electron region, both of which can remove some particles from the central peak.

4.3.3 Resonance shape

A series of fixed frequency measurements were made around the center of the resonance for the cooled and uncooled beam. Fig. 4.11 shows the resonance curves for these two cases, where each point is the average value of the polarization oscillation while the rf solenoid is on.

For the cooled case, the calculation of Fig. 4.11(a) was made using only a single particle track with no synchrotron amplitude because the inclusion of a full distribution as in Fig. 4.10 makes no signficant difference (< 0.003) in the resulting average polarization. The strength of the rf solenoid was 4.43×10^{-6} rev/turn and the ramp-up time was 200 ms. The calculated width is narrower compared to the data points.

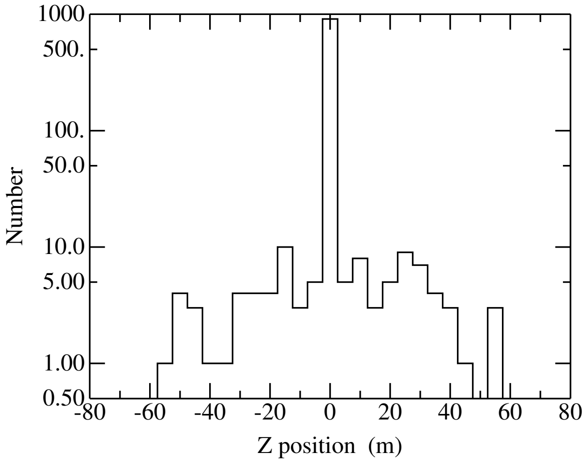

Figure 4.10: Synchrotron amplitude distribution for the cooled beam shown in Fig. 4.3.

For the uncooled case, the average polarization was taken to be the mean value after damping for about 0.5 s. Indeed, the solenoid strength was 2.66×10^{-5} rev/turn, its maximum value, and this caused the oscillation pattern to damp quickly. The ramp-up time for the rf solenoid was 200 ms. The model calculation was based on the amplitude distribution shown in Fig. 4.7(b) and used to reproduce the oscillation pattern of all the data points shown in Fig. 4.11(b). Here the level of agreement is mixed, with some calculations appearing above their respective data points and others below. The center of the resonance is placed at 871434 Hz. A finer adjustment was not possible because the frequency of the polarization oscillations is not well determined and in any case depends in the distribution of synchrotron amplitudes included in the calculation. Points whose average polarization is less than 0.5 suggest the resonance position should be slightly higher while those with a larger average suggest the opposite.

The shape of the resonance in Fig. 4.11(b) appears to be a “V” with gently curving sides. This shape is a consequence of the definition of the average polarization that makes up the data points. If instead the shape is taken to be the polarization at a specific time during the scan or the result at the end of the scan [23], then the shape will be different. On a very close inspection, the shape is in fact parabolic at the bottom point of the “V”. The scale of these graphs is not sufficiently expanded to reveal this feature, but it is more evident in Fig. 4.11(a).

In the attempt to reproduce the data points shown in Fig. 4.11, a lot of features of the resonance curve have been observed. This comparison made a strong test of the simple “no lattice” model used here. A short list is

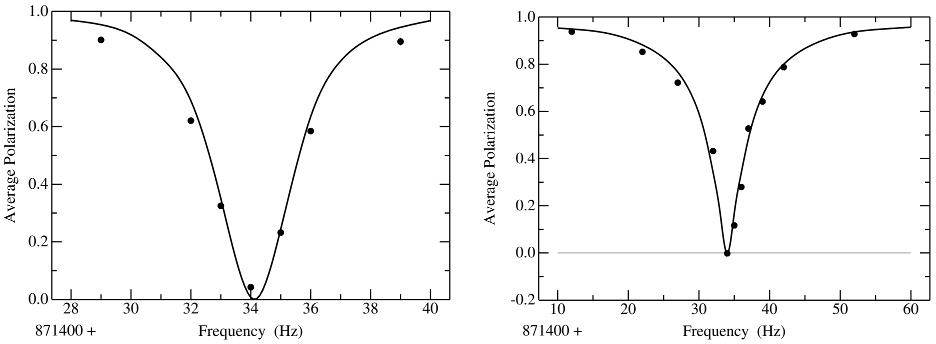

(a) (b)

Figure 4.11: The resonance curves for the cooled (see Fig. 4.11(a)) and uncooled (see Fig. 4.11(b)) cases. The solid line represents the model calculation while the black circles are the data points.

given as follows to summarize the results:

- at a particular frequency, the average value of the polarization is lower for a stronger rf solenoid field and a faster ramp-up time. This causes the resonance curve to be wider. The opposite situation appears for a weaker rf solenoid and a slower ramp-up time.

- there is a dependence on the distribution of synchrotron amplitudes. Variations in the trend of the reproduction may reflect changes in the amplitude distribution for the uncooled case from run to run. Each run, which corresponds to one data point, took about one hour to accumulate.

- during the experiment it has been observed that after the solenoid was ramped down, the average polarization for the uncooled beam rose to a more positive value. In general, the model also contains the same feature, but the amount of rise was not well reproduced. Like the effect of ramp-up time, the amount of rise depended on the ramp-down time. An investigation with different calculated ramp-down times showed that the dependence on this time was exponential (like the final value of the polarization in a Froissart-Stora scan) but did not offer any clear clues to the values of the exponential slope nor the final value of the polarization. A more detailed analysis is needed.

4.4 Conclusions

This study resulted from the attempt to measure depolarizing effects on the shape of the RF-solenoid spin resonance. Two choices in the setup, the use of a harmonic of the resonance because of the requirements on the operation of the RF-solenoid and the choice of bunching the beam on the first harmonic, led to the contribution of large amplitude synchrotron oscillations in the uncooled beam to the evolution in time of the vertical polarization. These contributions contain tracks that reflect an effectively weakened RF-solenoid and consequently have a longer oscillation period, even on-resonance. For the uncooled beam, this substantially changes the response of the system, creating a damped oscillation in the vertical polarization in the place of the continuously running oscillation observed for the cooled beam. These damped oscillations are built up of precession curves for the individual particles that continue to oscillate between a vertical polarization of +1 and -1. Compared to the on-resonance particle with no synchrotron amplitude, the oscillations in this set of functions have lower frequencies. This makes them different from the oscillations observed by moving the RF-solenoid frequency away from the resonance. In this case, the oscillations away from the resonance are characterized by higher frequencies and smaller amplitudes that cover a maximally positive range. Thus these two phenomena are distinguishable by the character of the damped oscillation.

The effects of transverse emittance or momentum spread were not directly or unambiguously observed during the experiment. Pursuing this further requires that we look directly at the spin decoherence of a horizontally polarized beam by unfolding the precession of the spin from the polarimeter measurements using time stamps associated with each polarimeter event. Such a stamp would allow us to locate it in the precession history of the beam since the inception of any spin manipulation within the beam store. This study is the subject of the next chapter.

Chapter 5

Spin Coherence Time measurements

The goal of the experiment presented in this chapter was the measurement of a rapidly rotating horizontal polarization as a function of time, made possible by the development of the data acquisition system explained in Sec. 3.2. The fitting procedure used to calculate the amplitude of the down/up asymmetry creates a positive offset of the measured polarization magnitude a low asymmetry. For this reason a section is dedicated to the method for correcting the model for this systematic effect and, at the same time, providing the definition for and extracting the spin coherence time (SCT). In the preliminary tests presented here, the vertical polarization was moved into the horizonal plane using an rf-solenoid running at the resonance frequency $f_{cyc}(1 - G\gamma)$ (as explained in the previous chapter). The horizontal polarization lifetime was then measured for different values of horizontal beam emittance and different setting of the sextupole magnets.

5.1 Exprimental setup

The new DAQ system was developed for the beam time of May 2012. The experiment was run with a bunched beam at the first harmonic and with momentum $p = 0.97$ GeV/c as for the measurements discussed in the previous chapter. But the available polarization states were only three: vector V(+), vector V(−) and unpolarized. The measured asymmetries ϵ_y gave a polarization down by more than a factor of three compared to sets of data shown in Chap. 4. Then a a better polarization was measured when making the substitution of the vector V(+) state with a tensor-vector state. It improved the vertical polarization of a factor of two and hence it has been used for the analysis presented here.

The goal was to study separately the size of the emittance effects in both X (radial) and Y (vertical) directions. But it proved difficult during the run to find a machine condition where the vertical emittance could be varied by itself (through electron cooling and then selective heating with white noise on electric field plates) while keeping the beam bunched. However, this was possible in the horizontal direction. So that degree of freedom was explored. Extraction of the beam was made through a vertical steering bump that brought the beam close to the thick polarimeter target. This helped to keep the size of the vertical emittance small so that changes could be related to the horizontal profile. The horizontal polarization was obtain by swithing the solenoid on for few seconds on resonance, such that it could flip the polarization and stop it in the horizontal plane.

The next step was to test a possible correction of the emittance effects by using sextupole magnets. In the COSY arcs there are two sextupole familes, groups of four magnets, MXS and MXL, which are located respectively where the β_x and β_y functions are large. Due to the machine tuning problems discussed above, only the effects of the MXS family were studied on a beam with a large horizontal emittance.

5.2 Extracting spin coherence time with correction of the systematic positive bias

Figure 5.1 shows horizontal polarization asymmetries measured for small to large horizontal beam profiles. As the profile becomes larger, the horizontal polarization lifetime shrinks because of the larger spread in spin tunes. The measured data (open circles) are subject to a positive bias since fitting a sine wave (see Sec. 3.2) with an undetermined phase to a random distribution always produces a non-zero magnitude. An initial correction for this effect produced the solid data points in Fig. 5.1 but a better method [26] (developed by E. J. Stephenson) that also determines the spin coherence time is described as follows. The time dependent shapes shown in Figure 5.1 are neither Gaussian nor exponential, so a numerical template was matched to the data in order to characterize the shape with a value of the spin coherence time. This also allowed for the correction of the systematic positive bias to be applied to the template, a procedure that is much better defined

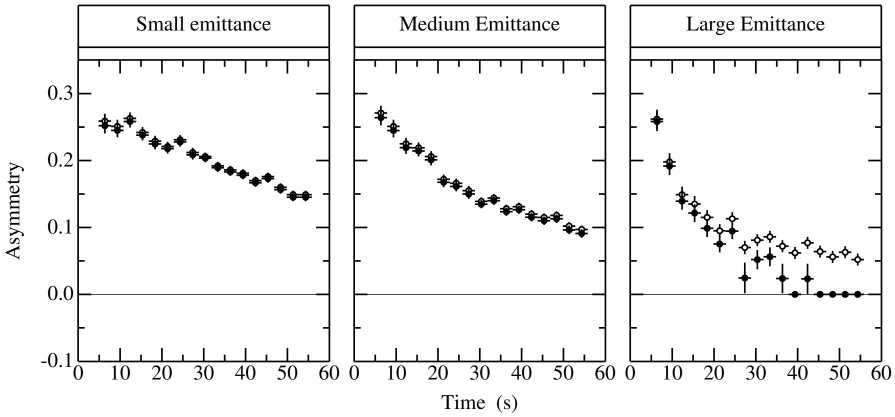

Figure 5.1: The three panels show horizontal polarization asymmetries measured for small, medium and large horizontal beam profiles respectively. As the profile becomes larger, the spin coherence time shrinks. A positive offset of the measured data (open circles) at low asymmetry comes from the fitting process using of a sine wave with an undetermined phase to reproduce a random distribution. An initial correction for this effect produced the solid data points. Overcorrections to magnitudes less than zero were replotted at zero.

than substracting the bias the asymmetry measurements directly.

Template curve $F_\alpha(t)$ The template assumes that the spread of spin tunes is due solely to the path lengthening (see Sec. 2.1.3) associated with the finite ϵ_x and ϵ_y emittances of a bunched beam. At any point in the ring with known beta functions, the emittance may be characterized by the angles θ_x and θ_y that represent the maximum deviation from the direction of the central orbit (see Eq. 2.14) at the location of the rms deviation of the distribution. The change in spin tune depends on the combination $\theta_X^2 + \theta_Y^2$ for each particle track. The values for θ_x and θ_y were chosen from two separate Gaussian distributions, each characterized by a width, σ_x and σ_y. Changing these widths relative to one another alters the time-dependent shape of the template curve, which may then be characterized by a new parameter $\alpha = \sigma_y/\sigma_x$. A change to the spin coherence time itself is equivalent to rescaling the time axis t of the template curve, $F_\alpha(t)$. During the experiment, it was possible to make σ_x, originally reduced through electron cooling, wider by applying white noise to a set of horizontal-field electric plates. Thus all tests were made with horizontal ribbon beams whose cross-sectional shape represented cases with $\alpha < 1$.

The template shapes were constructed by taking 10^6 spins and distributing them around a unit circle (in the storage ring plane) in accordance with the spin tune model just described for a particular value of α. An example of such a distribution for 300 spins and a single non-zero emittance is shown in Figure 5.2(a). At $t = 0$ all of the spins were at (X,Y) = (0,1) and the beam represented by this ensemble was completely polarized (p = 1). As time increases, the points revolve around the unit circle in one direction (increasing spin tune) since the quadratic sum of the angles is always positive. The distribution was allowed to spread linearly with time. At each time point, the X and Y components of the polarization were calculated, and the total polarization determined by adding these components in quadrature. For the single distribution case ($\alpha = 0$), the resulting polarization time dependence is the solid curve $F_0(t)$ in Figure 5.2(b). For larger values of α with σ_y fixed, the template curve falls more quickly, as shown by the broken curves in Figure 5.2(b).

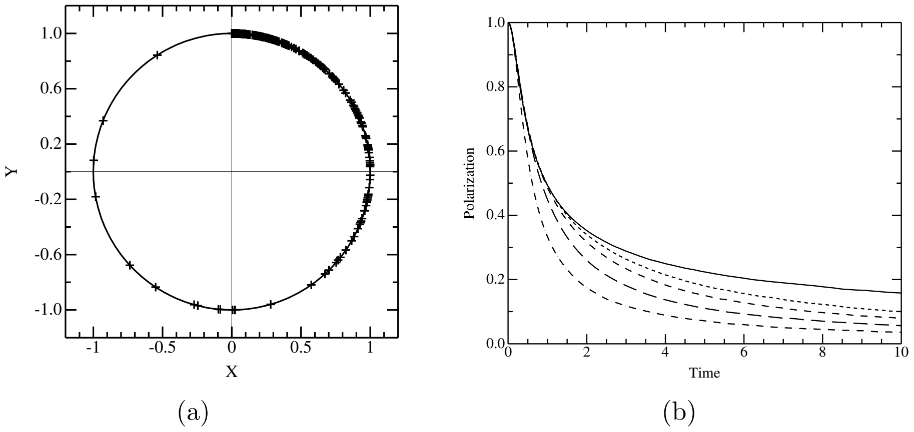

(a) (b)

Figure 5.2: Figure 5.2(a) shows the unitary circle in the XY plane where the spin are distributed following the square of a Gaussian distribution. It represents the spin positions in the plane at one time. Figure 5.2(b) shows five example of the numerical function used to describe the horizontal polarization as a function of time. These curves have the same properties except for the α value which is equal to 1, 1/2, 1/3, 1/4 and 0 (starting from the bottom). $\alpha = 0$ means that the beam is horizontal and flat because the vertical size becomes. $\alpha = 1$ is a round beam, the case in which the beam emittance effect on polarization is the largest.

Spin coherence time The initial departure of the template shape from one at small times is quadratic and in this respect like a Gaussian function. We chose as the “spin coherence time” the width at $p = 0.606$, the same value that corresponds to the amplitude of a Gaussian function whose argument is the function’s width σ. In order for this to work for the double distributions represented here, it is necessary to scale the template curve according to $F_\alpha(\sqrt{1+\alpha^2}\,t)$. The curves in Figure 5.2(b) include this scaling and remain well-matched to each other down to $p = 0.6$. Other parameters were included in order to match individual sets of asymmetry measurements and produce the adjustable template:

$$\begin{aligned} f(\alpha, t) &= a_1 F_\alpha(t_{\text{tab}}) \\ t_{\text{exp}} &= a_2\sqrt{1+\alpha^2}\,t_{\text{tab}} + a_3 \quad \text{where} \end{aligned} \tag{5.1}$$

- a_1 scales to match the asymmetry at the start of the horizontal polarization measurement;
- a_2 is proportional to the spin coherence time;
- a_3 is a time shift used to synchronize the template with the start time in the data stream.

The numerical lookup table is based on a fixed array t_{tab} whose interpretation as experimental time t_{exp} is given by the second line in Eq. 5.1. The factor $\sqrt{1+\alpha^2}$ decouples a_2 from the particle distribution in the transverse directions and thus provides a consistent definition for the spin coherence time indipendently from the shape F_α. The matching of the template to each data set was done with a numerically-driven non-linear regression routine.

In order to convert a_2 into the spin coherence time a scale calibration is needed. As was mentioned at the beginning of this paragraph, the initial behavior of the template curves follows a Gaussian function whose width is the spin coherence time. The value of t_{tab} at which the template curves cross $p = 0.606$ is the convertion factor called *index* and equal to 125.43. Finally, the spin coherence time can be obtained by multiplying a_2 times the *index* value.

Bias correction Let's consider the procedure to extract the horizontal polarization as a function of time described in Sec. 3.2. The amount of positive bias in the extraction of the amplitude of a sine wave representation of the 9 asymmetry points around the horizontal plane depends on the size of the statistical errors in the 9 points. These errors are typically similar for all bins, and a single average value is used. The value of the positive bias is the average magnitude of the sine wave fit to data with a random and a signal component minus the signal component. The larger the error, the larger is the positive bias. This effect is shown in Figure 5.3(a) where each axis is plotted in units of the typical error in a single angle bin. Below one, this bias becomes large. It is approximately, but not exactly hyperbolic, so the numerical table represented by Figure 5.3(a) was used to calculate the correction in each case. The asymmetries shown in Figure 5.1 represent an average over typically 15-20 storage cycles at COSY. While the error on the average becomes smaller, the bias remains the same. For each template shape and data point, the bias was calculated knowing the individual angle bin error and applied to the template curve. An example is shown in Figure 5.3(b) by the solid curve in comparison to the original template shape as a dashed line. A set of eleven template curves were generated for a range

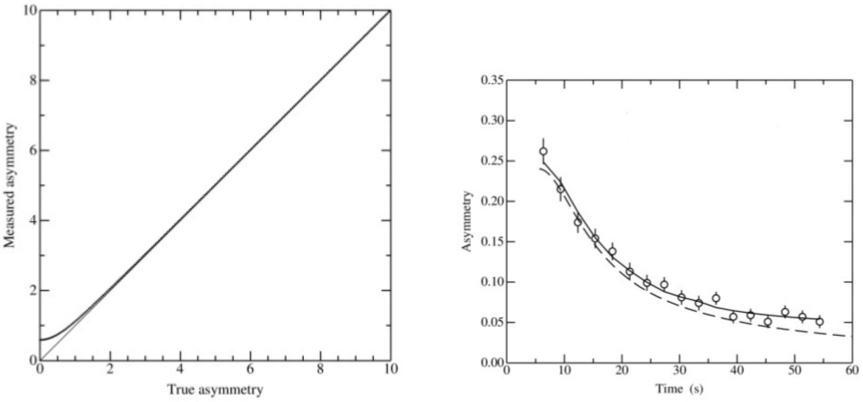

(a) (b)

Figure 5.3: Figure 5.3(a) shows a Monte Carlo simuation relating the observed asymmetry to the real asymmetry. The asymmetry scale is adjusted so that it represents the size of the statistical error in one angle bin for one time bin in one store. The positive bias problem becomes evident when the real asymmetry goes to zero and the error is about the size of the typical signal. Figure 5.3(b) is an example of the correction for a real case. The empty circles are the uncorrected data. The real polarization which corresponds to the data is represented by the dashed line. The real polarization with the positive bias included is the solid line.

of α values between 0 and 1. Non-linear regression fits were made for each template, and the final value of the spin coherence time taken from the one with the smallest reduced chi square. In general, this correlated well with changes in the ribbon beam shape during the experiment. Additional error contributions from the fitting process were added to the statistical errors when quoting the final spin coherence time. An example of the fitting procedure is shown in Fig. 5.4. On the top left corner, the experimental data represented by the balck dots are fitted with a non-linear regression routine for each template curve. The quality of these fits is given by the value of the reduced chi square which is plot for each α in the graph on the top right corner. The minimum of the quadratic curve fitting the reduced chi square points corresponds to the best value of α and is shown by a vertical solid red line. The horizontal dashed red line is the standard deviation width for this chi square curve. In the bottom of Fig. 5.4, there are two graphs representing the values of the parameters a_1 and a_2 resulting from the matching of the templates curves to the data set. In both cases, the red star represents the parameter value corresponding to the best α. The vertical error bars are calculated from the fitting porcedure and the statistical errors. The horizontal error bars of the red stars represent the width of the chi square curve. In the example shown here, the best value of α is 0.35 ± 0.05, the fitting parameters are $a_1 = 0.218 \pm 0.007$ and $a_2 = 0.080 \pm 0.005$ and the spin coherence time is $\tau_{SCT} = 10.0 \pm 0.6$ s. The finale curve produced by the analysis is shown with a solid red line in the top left graph of Fig. 5.4.

5.3 Emittance effects

There are two kinds of contributions to the spin tune spread from beam dynamics:

- at first-order, the spin tunes spread because of the spread of particle momenta described by the momentum distribution of $\Delta p/p$, where p is the reference value. This is removed by bunching the beam.
- a second-order contribution appears due to betatron oscillations that occur when beam particles oscillate about the central trajectory. Since bunching the beam keeps all particles on average isochronous, such oscillations lead to a longer beam path, a higher particle speed, and a change in the spin tune, as explained in Sec. 2.1.3.

The change in path length goes as the square of the maximum angle of deviation from the central ray. Then, it is expected that the reciprocal of the spin coherence time should go as the square of the width of the beam profile

$$\frac{1}{\tau_{SCT}} = A\langle\theta_x^2\rangle + B\langle\theta_y^2\rangle, \tag{5.2}$$

as appears to be the case in Fig. 5.5.

As already mentioned in the first section, the vertical emittance was kept small while only the horizontal emittance was varied for the tests. Fig. 5.5

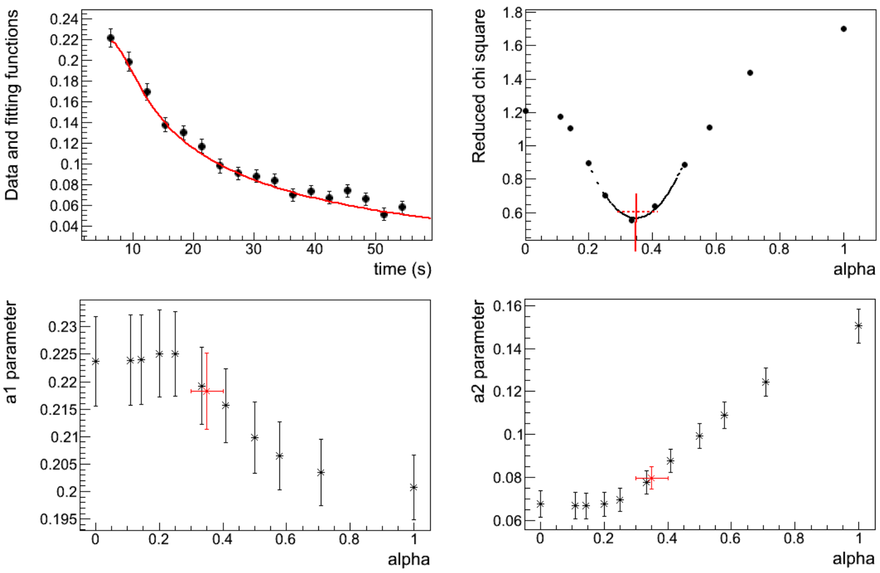

Figure 5.4: The four graphs show an example of the fitting procedure to calculate the spin coherence time. Starting from the top left corner, the experimental data are the balck dots and the solid red line is the final result of the analysis. In the right panel, the reduced chi square resulting from the fitting procedure of the template curves is plotted against the corresponding α value. The best α (shown by a vertical solid red line) is determined by the minimum of a quadratic curve fitting the reduced chi square points. In the bottom graphs, the values of the fitting parameters a_1 and a_2 are shown for each α. The red stars in these plots are the a_1 and a_2 values corresponding to the best α. For this set of measurement, the best value of α is 0.35 ± 0.05, the fitting parameters are $a_1 = 0.218 \pm 0.007$ and $a_2 = 0.080 \pm 0.005$, and the spin coherence time is $\tau_{SCT} = 10.0 \pm 0.6$ s.

shows a set of measurements for several horizontal profile widths (solid points). The vertical axis is the horizontal polarization lifetime, here chosen to be the time required for the beam to lose 1/3 of its initial polarization. The horizontal axis is the average beam profile Gaussian width in mm. Both quantities represent values from a preliminary analysis during the experiment. All of these were taken with electron cooling off, following a period with cooling on to reduce the phase space size with another short period of heating to expand the space horizontally. This gave profile sizes typically larger than 4 mm. A single point at 2 mm (star) was taken with cooling running continuously through the measurement.

Fig. 5.6 shows two example of horizontal polarization for a narrow (see Fig. 5.6(a)) and a wide (see Fig. 5.6(b)) beam. It is clear the emittance

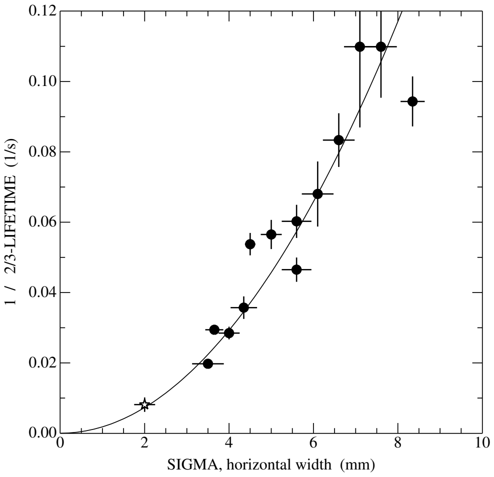

Figure 5.5: Measurements of the reciprocal of the horizontal polarization lifetime, here chosen to be the time required for the beam to lose 1/3 of its initial polarization. The horizontal axis is the average beam profile Gaussian width in mm. Both quantities represent values from a preliminary analysis during the experiment. Only the point with the star was measured with electron cooling running during data taking. The solid line represents a guide to the eye with a parabolic function.

effect on the spin coherence time, which is 50.0 ± 2.5 s in the first case and 5.5 ± 0.6 s in the second one.

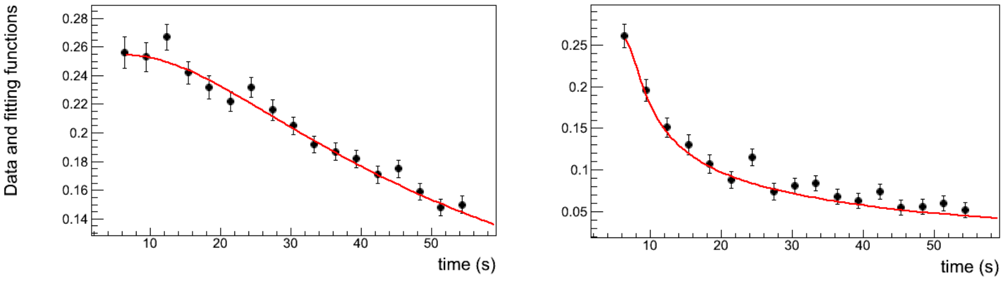

(a) (b)

Figure 5.6: Comparison of the horizontal polarization as a function of time for a narrow beam (see Fig. 5.6(a)) and a wide beam ((see Fig. 5.6(b)). It is evident how emittance affects the spin coherence time, which is 50.0 ± 2.5 s in the first case and 5.5 ± 0.6 s in the second one.

5.4 Sextupole corrections

Sextupole magnetic fields, which vary as the square of the radius from the center, can provide an adjustment to the particle orbit to remove the term driving the change in spin tune. Starting from Eq. 5.2, the sextupole corrections can be added as follows:

$$\frac{1}{\tau_{SCT}} = A\langle\theta_x^2\rangle + B\langle\theta_y^2\rangle + (c_1 J + d_1 K)\langle\theta_x^2\rangle + (c_2 J + d_2 K)\langle\theta_y^2\rangle, \tag{5.3}$$

where J and K are sextupole currents for magnets installed respectively where the β_x and β_y functions are separately large. In order to find the sextupole corrections to cancel the emittance effects on the spin coherence time, the system to solve is given by setting $1/\tau_{SCT}$ to zero:

$$\begin{pmatrix} J \\ K \end{pmatrix} = -\begin{bmatrix} c_1 & c_2 \\ d_1 & d_2 \end{bmatrix}^{-1} \begin{pmatrix} A \\ B \end{pmatrix} \tag{5.4}$$

where A, B, c_i and d_i with $i = 1, 2$ are coefficients to be determined experimentally. The idea is to measure the spin coherence time while varying J and K separately for different value of θ_x and θ_y.

During the beam time in May 2012 we used a setup with one of the larger horizontal beam profiles and the horizontal polarization lifetime was measured as a function of the setting of the MXS magnet strength (located where the β_x function is large). The strength, called K_2, is defined as:

$$K_2 = \frac{1}{B\rho}\frac{\partial^2 B}{\partial x^2}, \tag{5.5}$$

where B is the magnetic field and $1/\rho$ is the curvature. This reduces Eq. 5.3 to:

$$\frac{1}{\tau_{SCT}} = (A + c_1 J)\langle\theta_x^2\rangle, \tag{5.6}$$

where J corresponds to the sextupole strength K_2.

An initial investigation showed that changes were capable of lengthening the polarization lifetime. In contrast to the data shown in Fig. 5.5, the measure of the lifetime is changed to the spin coherence time . The results are shown in Fig. 5.7 which plots the reciprocal of the spin coherence time ($1/a_2$ scaled to 1/seconds) as a function of the strength of the MXS sextupole magnets. If the magnet strength increases beyond the point where the 1/SCT becomes zero and the spin tune spread is canceled, then a finite

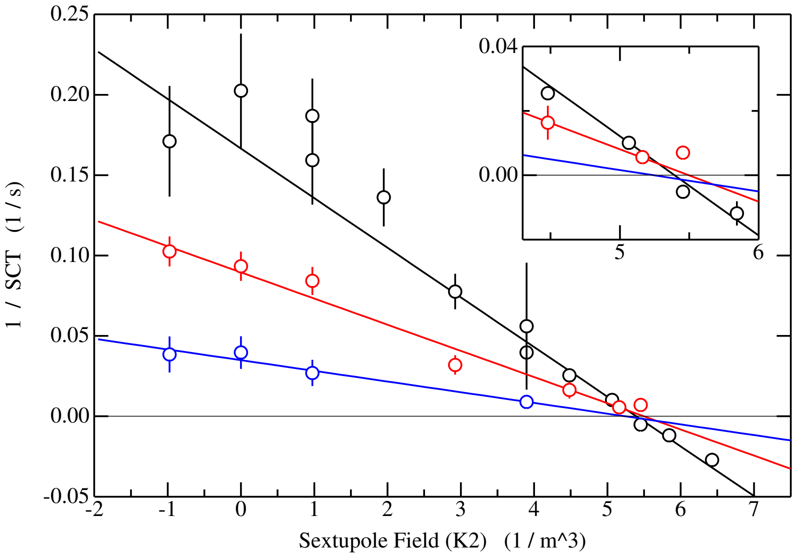

Figure 5.7: Measurements of the reciprocal of spin coherence time. The horizontal scale is the sextupole magnetic field strength. The three lines correspond to three different beam profile widths, starting from a narrow (bottom, blue) to a wide (top, black) profile. In order to determine wether this behavior is linear, all the points above the zero crossing at 5.4 ± 0.1 m^{-3} were reversed in sign.

polarization lifetime will return. In order to determine whether this behavior is linear, it is necessary that the 1/SCT values on one side or the other of such a zero crossing be reversed in sign. In Fig. 5.7, this was done to all of the points above 5.4 m^{-3}.

Changing the value of the sextupole field has a dramatic effect on the horizontal polarization lifetime. This approaches infinity as the 1/SCT goes to zero. The linearity of the effect comes from the matching of the quadratic sextupole field as a correction to the quadratic path lengthening, a function of the size of the horizontal emittance. Over most of this range, the dependence is clearly linear (after correction of the sign). The lack of distortions in the linear behavior near value of zero points to the lack of other contributions to shortening the polarization lifetime. Such contributions could come from the vertical beam emittance or couplings to the momentum spread.

Cooled beam Another test was made to measure the horizontal polarization lifetimes by cooling the beam for all the storage time, since it represents the case where the particle momentum distribution and emittances are the smallest. The beam was extracted onto the EDDA thick carbon target

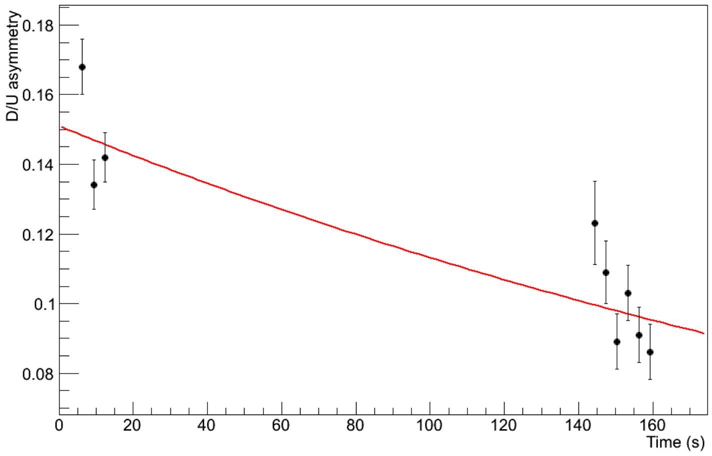

Figure 5.8: Measurements of the spin coherence time for a electron cooled beam. This represents the longest polarization lifetime recorded and corresponds to 316 ± 40 s.

for only a short time at the beginning and end of the horizontal polarization window, as is shown in Fig. 5.8. Under these conditions, the longest polarization lifetime recorded is 316 ± 40 s for the time required for the polarization to fall to $1/e$ of its initial value.

5.5 Conclusions

The goal of this set of experiments was to provide a demonstration that sextupole fields in a storage ring may be used to reduced the spread of spin tunes in a horizontally polarized deuteron beam. Such a demonstration is a critical part of showing that it is possible to build a special storage ring dedicated to the search for an Electric Dipole Moment (EDM) on charged particles. In order to have a sensitivity to the deuteron EDM that is about 10^{-29} e·cm, the spin coherence time should reach 1000 s.

The spin coherence time studies presented here confirm that the proper choice of sextupole fields could be used to preserve the polarization for times up to 1000 s. The correction illustrated in Figure 5.7 is for the one-dimensional problem, fixing a large horizontal emittance and spin tune spread with a sextupole located at a place with a large horizontal beta function. The zero corssing point represents the condition in which the spin tune spread due to the horizontal emittance is cancelled and it happens for a sextupole field strength of 5.4 ± 0.1 m^{-3}. In general, both X and Y emittance must be corrected. The MXL sextupole family is located where the vertical beta function is large, and is thus the right choice for the Y dimension. It is expected that the cancellation will require a consideration of the cross terms, MXS changing Y and MXL changing X. This study is left for the future.

It is also demonstrated that a long horizontal polarization lifetime (316 ± 40 s) can be achieved in the case of a cooled beam, since it represents the case where the particle momentum distribution and emittances are the smallest. Although this result is promising as it approaches the goal value for dedicated EDM measurements, the adopted cooling technique, making use of the electron cooler, cannot be directly applied to the final experiment as the magnetic fields used in the electron cooling system would destroy the EDM signal. As a possible alternative, the use of stochastic cooling has been proposed, but the effect of the stochastic cooling system on the spin dynamics of the stored beam has to be both theoretically and experimentally investigated.

Chapter 6

Conclusions

This thesis is part of the feasibility studies for a search for an Electric Dipole Moment (EDM) of charged particles in a storage ring. The evidence for a non-vanishing EDM at the sensitivity of present or planned experiments would clearly prove the existence of new CP violating meachanisms beyond the Standard Model. The proposed solution to measure the EDM of charged particles is the use of a storage ring where the polarized charged particle beam can be kept circulating while interacting with a radial electric field. Starting with a longitudinally polarized beam, the EDM signal would be detected as a polarization precession starting from the horizontal plane and rotating toward the vertical direction. A long horizontal polarization lifetime is required since it represents the time available to observe the EDM signal. In order to have a sensitivity to the deuteron EDM that is about 10^{-29} e·cm, the spin coherence time should reach 1000 s while the measurement of a vertical polarization change should detect angles as small as micro-radians.

The aim of this work is the analysis of the mechanisms which control the spin coherence time in a storage ring. The measurements presented here were made at the COSY (COoler SYnchrotron) ring located at the Forschungszentrum-Jülich GmbH (Germany).

There are two set of measurements presented in this thesis: the first is a study of an rf-solenoid induced spin resonance and the second shows the results from the first direct measurement of the horizontal polarization as a function of time.

The first experiment sought to estimate the spin coherence time by measuring the width of a deuteron spin resonance induced by an rf-solenoid. Since the width of the resonance depends on the spin tune spread and thus on particle momentum distribution, each mechanism that can change the particle velocity in the beam could contribute to the spin tune spread. In particular, these mechanisms are betatron oscillations which are due to the beam emittance and synchrotron oscillations that are present only in a bunched beam. In order to enphasize the dependence on the momentum distribution, several tests were made using a bunched polarized deuteron beam, either uncooled or electron-cooled. Similar studies on induced spin resonances can be found in the literature but none of them provided a continuous measurement of the vertical polarization as function of time. It was expected to see the effects of betatron oscillations on the spin resonance width. Instead, the measurments showed the effect of synchrotron oscillations on the induced spin resonance, an effect that was large enough to hide any dependence on emittance.

The experiment consisted of vertical polarization measurements with the rf-solenoid running at fixed frequency on and off resonance, and for uncooled and cooled bunched beam. Beginning with the on-resonance case, the observed vertical polarization patterns were clearly different for the cooled and uncooled beam conditions. In the cooled case, long lasting oscillations were observed whose period depended on the rf-solenoid strength. The polarization flip was complete. In the uncooled case the oscillation damped, ending finally in a constant polarization value. Moving off resonance, the amplitude oscillation for a cooled beam was smaller and the frequency was higher compared to the on-resonance case. For the uncooled beam, the oscillations were still damped and the final polarization value became more positive the further the measurement was made from the resonance frequency.

In order to understand these behaviors, a simple “no-lattice” model was developed based on two rotation matrices for the spin precession about the vertical axis and the solenoid kick about the longitudinal axis, while synchrotron oscillations were included as simple harmonic motion. The model results showed that for a single particle undergoing synchrotron oscillations, the spin flips completely under the resonance condition but the oscillation frequency depends on the amplitude of the synchrotron oscillations, the larger the amplitude, the slower the frequency. This is a very important result because it means that the effect of synchrotron oscillations is to weaken the rf-solenoid strength.

The second experiment was the direct measurement of the horizontal polarization as a function of time, made possible through the development of a dedicated data acquisition system synchronized with the revolution frequency of the horizontal polarization. By changing the horizontal beam emittance with a white noise electric field, the measurements gave the first experimental evidence of a dependence of the spin coherence time on the horizontal beam size. The dependence is due to the path lengthening introduced by betatron oscillations which forces the particles to go faster in order to respect the isochronous condition in a bunched beam. A possible method to correct for emittance effects is to use sextupole magnets whose field varies as the square of the radius from the center, providing an adjustment to the particle orbit to remove the term driving the spin tune change. Indeed, it has been demonstrated that for a particular value of sextupole strength the contribution from the horizontal emittance was canceled, reaching a spin coherence time of a hundred seconds. The same study for the vertical emittance is planned for the future. The longest horizontal polarization lifetime was reached in case of a cooled beam, corresponding to a $1/e$ spin coherence time of 316 ± 40 s.

A fundamental requirement for the EDM experiment is to get a long a spin coherence time. The presented results provided a demonstration that sextupole fields in a storage ring may be used to reduced the spread of spin tunes in a horizontally polarized deuteron beam. Such a reduction would make possible spin coherence lifetimes of a hundred seconds, as represented here by measurements of the lifetime of the horizontal polarization. Such a demonstration is a critical part of showing that it is possible to build a special storage ring dedicated to the search for an EDM on charged particles. It is also demonstrated that the longest horizontal polarization lifetime can be achieved in the case of a cooled beam, since it represents the case where the particle momentum distribution and emittances are the smallest. The measurement of a spin coherence time of 316 ± 40 s is also a world record compared to the previous result obtained with electrons and positrons [27]. Although this result is promising as it approaches the goal value for dedicated EDM measurements, the adopted cooling technique, making use of the electron cooler, cannot be directly applied to the final experiment as the magnetic fields used in the electron cooling system would destroy the EDM signal. As a possible alternative, the use of stochastic cooling has been proposed, but the effect of the stochastic cooling system on the spin dynamics of the stored beam has to be both theoretically and experimentally investigated.

Bibliography

[1] A. G. Cohen, De Rújula and S. L. Glashow, Astrophys. J. **495**, 539 (1998).

[2] A. D. Sakharov, Pisma Zh. Eksp. Teor. Fiz. **5**, p. 32-35 (1967).

[3] B. Aubert *et al.*, BABAR Collaboration, Phys. Rev. Lett. **89**, 281802 (2002).

[4] J. Christenson, J. Cronin, V. Fitch and R. Turlay, Phys. Rev. Lett. **13**, 138 (1964).

[5] E. M. Purcell and N. F. Ramsey, Phys. Rev. **78**, 807 (1950). E. M. Purcell and N. F. Ramsey, Phys. Rev. **108**, 120 (1957).

[6] R. Peccei, in *CP Violation*, C. Jarlskog, ed., World Scientific, Teaneck N.J. (1989), p. 503.

[7] G. L. Kane, *Perspective on Supersymmetry*, World Scientific, Singapore (1988), p. XV. J. H. Schwartz and N. Seiberg, Phy. Mod. Rev. **71**, S112 (1999).

[8] J. M. Pendlebury and E.A. Hinds, Nucl. Instrum. Methods A **440**, 471 (2000).

[9] M. Pospelov and A. Ritz, in *Lepton Dipole Moments*, B. L. Roberts and W. Marciano ed., World Scientific, Singapore (2010), p. 439-518.

[10] P. Langacker, in *The Standard Model and beyond*, CRC Press, USA (2010), p. 400.

[11] J. E. Kim and G. Carosi, Rev. Mod. Phys. **82**, 557 (2010).

[12] C.P. Liu and R.G.E. Timmermans, Phys. Rev. C **70**, 055501 (2004).

[13] B.C. Regan, E.D. Commins, C.J. Schmidt and D. DeMille, Phys. Rev. Lett. **88**, 071805 (2002).

[14] C.A. Baker *et al.*, Phys. Rev. Lett. **97**, 131801 (2006).

[15] W. C. Griffith *et al.*, Phys. Rev. Lett. **102**, 101601 (2009).

[16] L. H. Thomas, Phil. Mag. **3**, 1 (1927). V. Bargmann, L. Michel and V.L. Tlegdi, Phys. Rev. Lett. **2**, 435 (1959). T. Rosers, in *Handbook of Accelerator Physics and Engineering*, A. W. Chao and M. Tigner ed., World Scientific, Singapore (2002), p. 150.

[17] D. A. Edwards and M. J. Syphers, *An Introduction to the Physics of High Energy Accelerators*, Mel Month ed., John Wiley & Sons Inc., USA (1993). S. Y. Lee, *Accelerator Physics*, World Scientific, USA (2004).

[18] P. D. Eversheim *et al.*, in AIP Conf. Proc., Vol. 339 (AIP, Woodbury, NY, 1995) p. 668; R. Weidmann *et al.*, Rev. Sci. Instrum. **67**, 1357 (1996).

[19] H. H. Barschall, Am. J. Phys. **35**, 119 (1967). S. E. Draden, Am. J. Phys. **35**, 727 (1967).

[20] N. P. M. Brantjes *et al.*, Nucl. Instrum. Methods A **664**, 49 (2012).

[21] D. Albers *et al.*, Eur. Phys. J. A **22**, 125 (2004). J. Bisplinghoff *et al.*, Nucl. Instrum. Methods A **329**, 151 (1993).

[22] Y. Satou *et al.*, Phys. Lett. B **549**, 307 (2002).

[23] V. Morozov *et al.*, Phys. Rev. Lett. **103**, 144801 (2009).

[24] M. Froissart and R. Stora, Nucl. Instrum. Methods **7**, 297 (1960).

[25] P. Benati *et al.*, Phys. Rev. STAB **15**, 124202 (2012).

[26] E. J. Stephenson, private communication.

[27] I. B. Vasserman *et al.*, Phys. Rev. B **198**, 302 (1987).